Aeroelastic Tailoring using the Spars and Stringers Planform Geometry

G. Francois[1], J. E. Cooper[2] and P. M. Weaver[3]
Department of Aerospace Engineering, University of Bristol, Bristol, BS8 1TR, U.K.

The aeroelastic performance of a wing, including static aeroelastic shape, flutter/divergence speed and gust load response, has a significant influence on aircraft design. The tailoring of aeroelastic responses therefore offers potential weight savings. In this paper, the spars and stringers planform geometry (i.e. shape and root/tip chord wise location) on a representative wind tunnel model aircraft wing are used to modify the wing aeroelastic performance. Several optimisations are performed to illustrate the ability of the spars and stringers planform geometrical features to change the wing vibrational mode natural frequencies, deformation under a static tip load and aerodynamic load, gust response and aeroelastic instability speed. Changing the stringers planform geometry is shown to offer minor variation in the wing deformation and loads. Changing the spars planform geometry is shown to enable a reduction in root bending moment under static aerodynamic loading greater than 10%, a reduction in maximum root bending moment encounter during a worst case scenario gust event greater than 10% and a 25% increase in flutter speed. The improvements due to a change in the spar planform geometry are compared to the effect of changing the wing sweep angle. A framework to characterise Euler-Bernoulli beam properties on wings with geometric coupling is then developed and validated to relate the stiffness and bend/twist coupling parameter to the full 3D FE models.

I. Introduction

The airline industry is expected to see a growth of 5% per annum for the next two decades[1]. In order to support such growth a number of challenges need to be tackled among which the industry‘s dependency on fossil fuel is one of the biggest. Aircraft designers and manufacturers are therefore looking at ways to reduce aircraft fuel consumption.

The science of aeroelasticity focuses on the deformation and response of structure under aerodynamic, inertia and elastic forces[2]. Applied to wing design, aeroelastic considerations can be used to control the wing shape during cruise flight, control the wing response to gust encounter and also prevent the instigation of flutter and divergence. Thus the control of aeroelastic properties of a wing could offer weight and fuel savings. This approach is known as aeroelastic tailoring[3].

The control of aeroelastic properties is achieved through the control and coupling of bending and torsion deflections. Such control has been principally achieved through the use of composite materials where the stiffness tailoring is achieved through the design of the fibre orientations[4–9].

More recently, research work[10–21] focusing on the development of lighter wing structure has shown that the use of novel wing structural designs can control the aeroelastic performance and reduce the wing structural mass. These results have been highlighted by research in wing structure topology which encompasses the study of the number, position, size and shape of structural features. However, common pitfalls in topology optimisations are: (1) the complexity of the solution produced is not readily transferable into real designs especially if composite materials are to be used as complex three dimensional shapes and ply drop-off are to be avoided, (2) the complexity of the solution produced means that it is hard to understand how aeroelastic tailoring was created and (3) the high dependency of the final result to the load cases and optimisation objectives considered imply that multiple load cases and objectives would need to be defined early in the design process. Thus it is hard to know when and how topology optimisation will be used in wing design. There is a need to consider how aeroelastic performance of a classical wing structure made of spars, ribs, stringers and covers can be improved.

[1] PhD Research Student
[2] Royal Academy of Engineering Airbus Sir George White Professor of Aerospace Engineering, AFAIAA
[3] Professor in Lightweight Structures

Work presented previously[22–30]on the effect of curvilinear structural members on the structural response of wings has shown that its effect is not negligible and could be a source of wing performance improvements. However, only limited work has been performed on simple, idealised structure necessary to understand the fundamental mechanisms by which the structural response is modified by changing the shape of the structural members. In addition, only limited work has considered optimisation of the structural shape of the wing purely in terms of aeroelastic tailoring and only a limited design freedom - whereby the leading edge and the trailing edge spars remained straight- has been considered.

Therefore, there is a clear need to further develop the understanding of the relationship between the wing internal structural members' geometry and the wing deformation through variations in the structural members' geometry of a representative wing structure made of spars, ribs, stringers and covers. In this effort, Francois *et al*.[31] showed the effect of changing the rib orientation and sweep angle on the wing deformation and response. Additionally, there is a need to translate this understanding into simple tools that designers can use in the early design phase to make a better judgement on the structural members' geometry.

Beam models have been extensively used to describe the capacity of composite materials to influence the bending and torsional deflections. Such models also characterise a wing structure deformation by using three cross-sectional stiffness parameter around a reference axis. According to Weisshaar[5], the bending moment (M) and torque (T) can relate to the bending (w'') and twist (θ') curvature along the beam reference axis using

$$\begin{bmatrix} M \\ T \end{bmatrix} = \begin{bmatrix} EI & -K \\ -K & GJ \end{bmatrix} \begin{Bmatrix} w'' \\ \theta' \end{Bmatrix} \tag{1}$$

where EI and GJ are the bending and torsional stiffness parameter and K is the bend/twist coupling parameter. When dealing with composite materials, K is a function of the material properties.

The interest and use of the beam model can be understood when considering the numerous advantages that the beam model offers to designers. First, such a model is easy to implement while providing a way to include the bend/twist coupling possibilities of a composite material and for this reason is often used in the preliminary design stage. Additionally, the use of a single term to characterise the bend/twist coupling capability of a stacking-sequence, K, offers designers a relatively simple comparison metric. Considering such advantages, there is a need to develop a frame-work to enable the identification of beam properties that can characterise geometric bend/twist coupling.

In this paper, the effect of varying the spars and stringers planform geometrical features (shape and root/tip location) on the wing static and dynamic structural response for aeroelastic performances is examined. In addition, the characterisation of the wing's bend/twist coupling and stiffnesses due to the structural members' geometry is related to a simple structural beam model.

II. Concept Explored, Wing Model Geometry and Modelling

A. Concept Explored

We consider the variation in the planform geometry (i.e. shape and root/tip chord wise location) of the spars and stringers as illustrated in Figure 1. An un-tapered wind tunnel model wing was chosen as a test case in this work as experimental studies of this wing geometry have also been performed elsewhere [32,33]; the underlying conclusions from the work is expected to scale up to a full-scale aircraft wing model. The figures illustrating the shape of structural elements have the spars, the ribs, the stringers, the wing aerodynamic limits and the wing flexural axis shown in red, blue, black, magenta and green respectively.

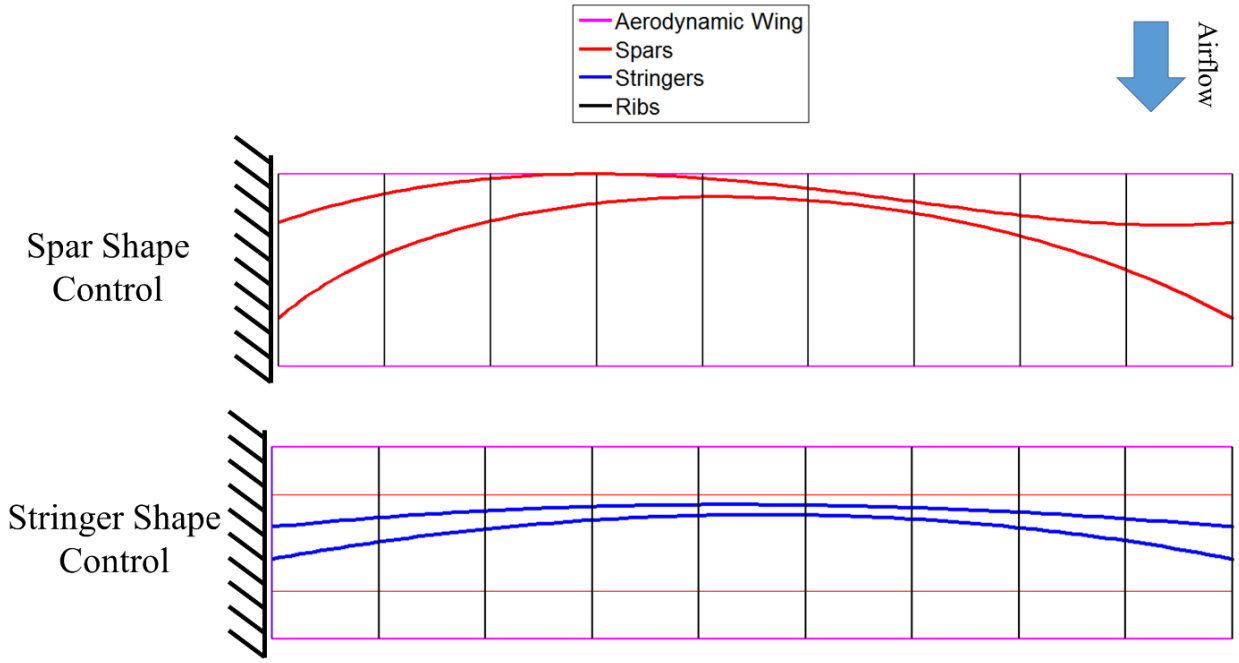

Figure 1. Illustration of the Structural Members Planform Geometry Variation Investigated in this Paper.

B. Wing Model Geometry and Material

The wing geometry used has a span of 500mm and a chord of 100mm as shown in Figure 2. The skin and spar thickness are 2mm and 4mm respectively. The wing's internal structure has 8 ribs, 2 spars as well as root and tip ribs. The leading and trailing edge spars are located at 25% and 75% of the wing chord, respectively. The wing box is of a constant thickness to chord ratio of 9.5%. The constant thickness to chord ratio was approximated by converting a NACA0012 profiled wing section into an equivalent rectangular wing box through the use of thin-wall beam theory and considering the second moment of area contribution of the different structural members.

The Baseline wing shown in Figure 2 has 4mm thick ribs. The rib thickness was varied for all other wing design considered to compare wings of similar mass.

When performing the spar geometry optimisation the wing does not have any stringers. When considering the effect of stringers shape, the Baseline wing is fitted with two square cross-section stringers in the top and bottom covers with length and height of 2mm.

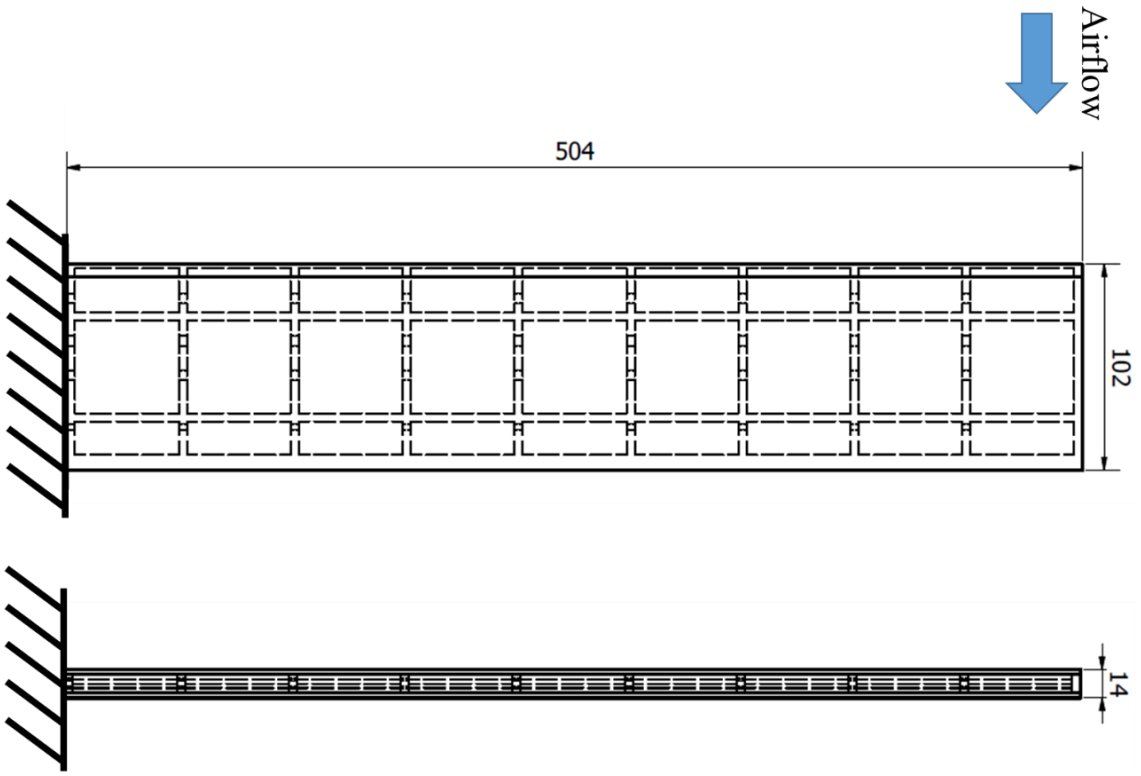

Figure 2. Wing External Dimensions in mm.

The wing was assumed to be made using a solidified polyamide material - a material used in previous experiments [32,33]- with a Young's modulus of 1,650.0MPa, a Poisson's ratio of 0.4 and a density of 1.15g/cm^3. The material was assumed to be isotropic and homogenous.

C. Finite Element Modelling

All wing models were analysed using Finite Element analysis (FE). A MATLAB routine which created a MSC.PATRAN session file for the different wing design considered was used. This file was then run in MSC.PATRAN and contained all the necessary actions to create an FE model such as the creation of the surfaces, meshing of the surfaces, node equivalence and check of the element geometries as well as the creation of element properties and boundary conditions to be used in the different analyses. IsoMesh and Paver meshing algorithms were used to mesh the wing models. The models used 2D shell elements (CQUAD) and the element geometry was checked to avoid highly skewed elements. If the elements were found to be highly skewed they were replaced by CTRIA3 elements using MSC.PATRAN mesh verification tool. The model mesh contained over 7,000 structural elements and 1,200 aerodynamic panels for the aeroelastic calculations. Mesh convergence studies were performed for each analysis performed. The stringers were modelled using 1D beam elements (CBEAM).

In order to quantify the variation in bend-twist coupling by the different concepts explored the position of the Flexural Axis is estimated for the wing boxes in FE modelling. In this paper, we assume that the flexural axis is the line connecting flexural centres which are a point on a wing section at which the application of a shear force creates no twist of that section with respect to the root [34,35]. The flexural centre of a section can be found by successively applying a small static load (MSC.NASTRAN SOL 101) at the leading and trailing edge of that section. These two analyses provides us with two twist angles of the section. Using linear interpolation the location of the flexural centre of the section can be found. The process is repeated for several sections.

D. Mass Control Method

The concepts are explored on a mass neutral basis where all wings considered have the same mass – the mass of the Baseline wing with stream-wise ribs and straight ribs, spars and stringers. The variation of the spars and stringers planform geometry can lead to longer spars and stringers compared to the Baseline wing. Thus to avoid an increase in wing mass, we chose to reduce the rib thickness accordingly. Figure 3 shows that the convergence of mass in FE is quick for the Baseline wing and for a wing with curved spars and ribs. Thus to calculate the necessary rib thickness

for a neutral wing mass, any wing design is run twice with a coarse mesh prior to the analysis run. In the first run the wing is run with the baseline rib thickness of 4mm and give a "heavy" wing mass. For the second run a reduced rib thickness is used. This reduced rib thickness is found by estimating the increase in the spars/stringers length. This second run gives a "light" wing mass. Having two masses with the two different rib thicknesses, the weight neutral rib thickness can be estimated using linear interpolation.

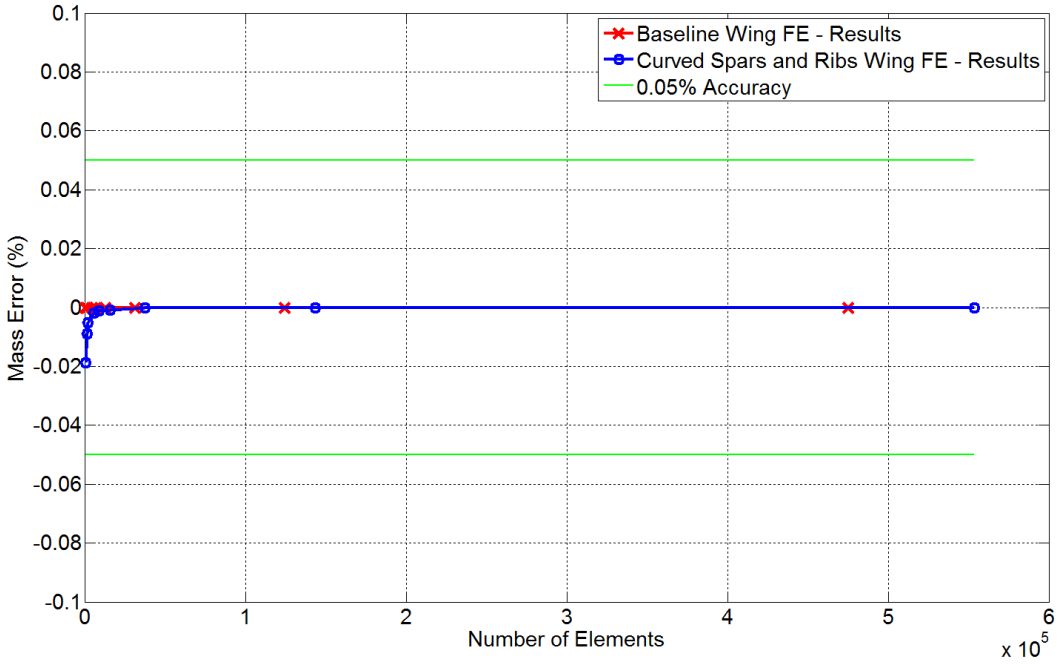

Figure 3. Wing Mass Mesh Convergence Study.

E. Curved Parametrisation

The wing structural members' position and shapes are controlled using Bezier curves - a polynomial representation method suitable for optimisation methods as it allows the control of the polynomial curves with only a limited number of control points. The polynomial curve is strictly defined by the control points thus limiting the number of decision variables making it an attractive method for optimisation purposes[36]. The Bezier curve representation can be expressed using the generalised formula shown in Equation 1 where the position of the control points permit the development of a polynomial equation used for shape parametrisation with n the number of control points, $\overline{P}_i$ the control points and $B_{i,p}(u)$ p order Bernstein polynomials.

$$\overline{R}_g(u) = \sum_{i=1}^{n} \overline{P}_i B_{i,p}(u) \tag{2}$$

The number of control points (n) is of $p+1$ for a shape polynomial of order p. In this work, only second and third order curves where used. For such purposes Equation 2 can be expressed in an explicit form shown in Equation 3, where t represents the number of points on the curve and P_i the control points coordinates.

$$B(t) = \sum_{i=0}^{n} \binom{n}{i} (1-t)^{n-i} t^i P_i \tag{3}$$

Using Equation 3 in two dimensions, a list of points with ordinate and abscissa values defining the position and shape of the spars and stringers are found. The depth direction for each point can be added by considering the profile of the wing box – a rectangle in this particular case.

III. Optimisation Method and Implementation

Since a wide variety of planform geometry for the different structural members had to be considered to improve aeroelastic performance this was a clear optimisation problem. The following section explains the optimisation method used and its implementation.

A. Optimisation Method Used

To perform the optimisation, an evolutionary optimisation method was used. Evolutionary optimisation methods mimics search and improved methods developed by Nature such as gene selection or bird flock motion. The optimisation chosen in this study was the Particle Swarm Optimisation (PSO) method as it uses continuous decision variables and can be used to find global optimal solutions for non-convex problems.

The PSO algorithm is a global stochastic search method that uses continuous decision variables originally derived by Kennedy and Eberhart[37]. The optimisation method is inspired from animals swarm movement where swarm particles remember their best value position as well as the best value position of the swarm. Each particle is assigned a position as well as a velocity on the search space. The velocity and position of each particles and the swarm is updated to the k^{th} iteration based on both the best values of each particles and the overall swarm best position using Equations 4, 5, 6 and 7.

$$x_i(k+1) = x_i(k) + v_i(k) \tag{4}$$

$$v_i(k+1) = \alpha v_i(k) + \beta \rho_i(k)\left(\overline{x}_i(k) - x_i(k)\right) + \gamma \sigma_i(k)(\overline{x}_{swarm}(k) - x_i(k)) \tag{5}$$

$$\overline{x}_i(k+1) = argmin\left\{f\left(\overline{x}_i(k)\right), f(x_i(k))\right\} \tag{6}$$

$$\overline{x}_{swarm}(k+1) = argmin\left\{f\left(\overline{x}_i(k)\right)\right\} \tag{7}$$

where x_i, v_i and $\overline{x}_i$ are the position, velocity and own best position of particle i, $\overline{x}_{swarm}(k)$ the swarm best position respectively. α, β and γ are user defined factors with given values of 0.75, 0.15 and 0.15 in this study. ρ and σ are random numbers between 0 and 1 generated independently for each particle.

B. Cost Functions

The aim of the optimisations was to find new internal structure geometries to vary the wing structural response. Several analyses were considered individually and for each a different cost function was formulated to improve a specific metric.

For the static tip load analysis the optimisation aimed at maximising the tip displacement and tip twist. For the static aeroelastic analysis, optimisations aimed at maximising and minimising the tip displacement and tip twist. When considering the natural frequencies, the optimisation aimed at maximising the natural frequencies of the different bending and torsion modes. Finally, when considering aeroelastic instability and the gust events, three different objectives were considered: (1) maximisation of the aeroelastic instability speed, (2) minimisation of the maximum root bending moment in a worst case scenario gust event and (3) finally a multi-objective optimisation of both (1) and (2).

For every wing a cost (J) was calculated which is made of ratio between the performance of the Baseline wing and the new solution. The Baseline wings performance metrics are summarised in Table 1 and Table 2. All Baseline wings undergo a flutter instability with a coalescence of the first bending mode (dominant), second bending mode and the first torsion mode.

Table 1. Baseline Wings Mass, Average Tip Displacement and Twist under Static Tip Load and Aerodynamic Load, Maximum Root Bending Moment during a Gust Encounter and Flutter Speed.

		Static tip load analysis		Aeroelastic analysis		Maximum Bending moment during a gust encounter (N.mm)	Flutter Speed (m/s)
Baseline Wing Model	Mass	Average tip displacement	Tip twist (°)	Average tip displacement	Tip twist (°)		
2 spars, 8 ribs	317.4	12.31	0	13.68	0.41	1655.65	117.91
2 spars, 8 ribs, 4 stringers	326.6	12.03	0	16.00	0.47	1658.87	118.21

Table 2. Baseline Wings Natural Frequencies and Mode Shapes (B: Bending Mode, T: Torsion Mode).

Baseline Wing Model	Natural Frequency (Hz) & Mode Shape									
2 spars, 8 ribs	11.21 (B)	66.99 (B)	68.02 (F/A)	73.72 (T)	175.04 (B)	220.86 (T)	313.83 (B)	359.13 (F/A)	366.94 (T)	469.39 (B)
2 spars, 8 ribs, 4 stringers	10.42 (B)	62.55 (B)	66.16 (F/A)	66.45 (T)	164.44 (B)	199.89 (T)	296.85 (B)	334.64 (F/A)	342.03 (T)	444.76 (B)

C. Decision Variables

The decision variable set to control the structural members varied based on which structural member groups were controlled (spars or stringers). The shape parametrisation decision variables were the Bezier curve control points for the structural members, with each control point having a specified position in both chord and span directions (X_i and Y_i).

Each structural members group was optimised assuming both "fixed end points" and "free end points". The "fixed end points" optimisations assumed that the starting (at the root) and ending points (at the tip) of a structural member were defined by the initial wing geometry and so were fixed to prevent root and tip motion. Hence in the "fixed end points" optimisations only the planform shape of the structural members are changed. The "free end points" optimisations assume that the starting and ending points chord wise location of the structural members are decision variables. Hence both the planform shape and the root and tip chord wise location of the structural members are optimised when using the "free end points" decision variable set.

The spars were fitted with third order Bezier curves. For the "fixed end points" optimisations only two control points were required for each spar making a total of 4*s* decision variables to control the spars shape of *s* spars. "Free end points" optimisations requires 6s decision variables.

The stringers were fitted with third order polynomials. Thus, only two control points were required for each stringers making a total of 4*p* and 6*p* decision variables to control the shapes of *p* stringers for "fixed end points" and "free end points" optimisation respectively.

In this paper each group were controlled and optimised individually. The decision variables for the different optimisation performed is summarised in Table 3.

Table 3: Summary of the Decision Variables Sets and Corresponding Number of Decision Variables for a Wing with *s* Number of Spars and *p* Number of Stringers.

Decision Variables Sets	Number of Decision Variables	
	"Fixed end points" Optimisations	"Free end points" Optimisations
Individual Spar Shape Control	4*s*	6*s*
Individual Stringers Shape Control	4*p*	6*p*

D. Penalty Functions

The PSO algorithm is a non-constrained optimiser hence if constraints are to be enforced the user must use penalty functions[38,39]. In this study, the constraints prevented certain optimisation pitfalls and aimed at reducing the design space to only structurally viable solutions. These constraints were hard constraints which must be met by every

solution considered. To allow for a quantification of how much the solutions were outside the correct design space a non-stationary penalty function was used. This penalty function, $h_1(x)$, is an aggregate metric of every broken constraint and are defined by

$$h_1(x) = \sum_{i=0}^{m} q_i(x) \tag{8}$$

where x is a design solution and $q_i(x)$ is a function describing a violated constraint. The $h_1(x)$ term was triggered when any of the geometry constraints were not respected. In order to avoid unnecessary calculations, the particles which triggered the penalty term $h_1(x)$ were not analysed using FE analysis and so the solution associated cost, $J(x)$, became the penalty term $h_1(x)$.

The geometry constraints checked that the geometry was feasible (i.e. spars/stringers not crossing each other and at appropriate distance from each other). The structure of the wing was also only allowed to move within the aerodynamic shape of the wing which was fixed throughout the optimisation process. Finally, the angle between the ribs and the spars was limited to a minimum of 10° so as to prevent highly skewed elements.

E. Optimisations Performed

In this paper, the average tip displacement is calculated by averaging the displacement at the tip leading and trailing edge. Nose up twist is shown by a positive twist value.

1. Static Tip Load Optimisations

The static load analysis was performed using MSC.NASTRAN SOL 101 assuming a leading and trailing edge tip load of 243.5g. The wings were assumed to be fully fixed at the root.

The static analysis optimisations aimed at maximizing the tip twist and tip displacement of the wing. For each decision variable set used six displacement maximisation and six twist maximisation optimisations were performed.

2. Natural Frequency Optimisations

The natural frequencies of the different mode shape of the wings were estimated using MSC.NASTRAN modal analysis (SOL 103). The wings were assumed to be fully fixed at the root.

The natural frequency optimisations aimed at maximising the natural frequency of the vibrational modes. Six optimisations aimed at maximising the natural frequencies of the first ten modes and six aimed at maximising the natural frequencies of the first five mode. Hence the results are split into two data sets for each decisions variable set.

3. Static Aeroelastic Optimisations

The static aeroelasticity analysis (MSC.NASTRAN SOL 144) was performed at an angle of attack of 5° and at a speed of 35m/s using a doublet lattice panel method. In this analysis the wing was assumed to be fully fixed at the root. The modelling was performed at an air temperature of 25°C similarly to the temperature experienced in the wind tunnel. A symmetry at the root is assumed to consider the reflection from the wind tunnel wall [40].

The results discussed were obtained from twelve different optimisations for each decisions variable set. Three optimisations aimed at maximising the tip displacement and three aimed at maximising tip twist. Finally three optimisations aimed at minimising the tip displacement and three aimed at minimising the tip twist. Hence the results are split into six data sets for each decisions variable set.

4. Aeroelastic Instability Speed and Gust Response Optimisations

The aeroelastic instability speed analysis was performed using MSC.NASTRAN PKNL analysis (SOL 145). The PKNL (PK No Looping) method is a PK method that uses direct matching of air speed, Mach number and air density at which to investigate the behaviour of the wing [40,41]. The analysis was performed with a range of Mach number from 0.01 to 0.5 with matching airspeed at sea level and at 25°C using a doublet lattice panel method. A symmetry at the root was assumed to consider the reflection from the wind tunnel wall [40]. The inclusion of 0.5% of structural damping prevented the triggering of soft flutter modes in the analysis [2,40].

The aeroelastic instabilities were found by tracking sign inversion of the modes damping values. The speed of the aeroelastic instabilities is found by linearly interpolating between the last speed with a positive damping value and the first speed with a negative damping value. The distinction between a flutter and a divergence instability was made by

tracking the imaginary part of the eigenvalue. If the imaginary part of the eigenvalue after the mode damping value switch was null the instability was divergence.

In the case of a flutter instability it is interesting to investigate the mode contributing to the flutter mode. To do so, the modal eigenvectors (modal participation factor) for each eigenvalue calculated during the PKNL analysis can be outputted. The modulus of each eigenvector, at the instability, can then be calculated to determine which mode contributes to the flutter mode.

Gust loads can be of crucial importance to aircraft designer as they can be the design loads for which the wing structure is sized. It is, therefore, important to assess the effect of the different concepts on gust loads. Various metrics can be used to assess this effect as explained in [42]. For this paper, considering that only the wing is considered and is assumed to be fully fixed during the analysis, the root bending moment generated during a gust encounter was chosen as the metric of interest.

Gust events are simulated assuming the gust velocity profile varies as '1-Cosine' using MSC.NASTRAN SOL 146 for which the time domain gust velocity is expressed using

$$w_g(T) = \frac{w_{g0}}{2}\left(1 - \cos\frac{2V\pi}{L_g}T\right) \tag{9}$$

with T the analysis time variable, ω_{g0}, the peak gust velocity and the gust length L_g [2]. The gust analysis was performed at sea level and at a speed of 35m/s at 25°C. A symmetry at the root was assumed to model the reflection from the wind tunnel wall [40]. A value of 0.5% of structural damping was used in this analysis. Six gust lengths were considered varying linearly from 0.7m to 7.0m with a peak gust velocity of 0.5m/s. The wing root is assumed to be fully fixed through a Multiple Point Constraint (MPC). The wing root bending moment was assessed by considering the bending moment created on the node slaving all the nodes at the root. The maximum root bending moment for a given wing design was found by fitting the root bending moments at each gust length using a Radial Basis Function (RBF) [42] method.

The results discussed were obtained from six different optimisations for each decisions variable set. Two optimisations aimed at maximising the first aeroelastic instability speed and two aimed at minimising the maximum root bending moment encounter during a worst case scenario gust event. Finally two optimisations aimed both maximising the first aeroelastic instability speed and minimising the maximum root bending moment encounter during a worst case scenario gust event. Hence the results are split into three data sets for each decisions variable set.

IV. Spars Planform Geometry

In order to provide a complete picture on the effect of the spar geometry on the response and deformation of a wing the optimisation results obtained are compared to the response and deformation of some swept wings in the following discussion. The results for the swept wings used in this section were presented previously in Francois *et al.*[31] and only consider swept wings with rib orientation parallel to the free stream. The mass of the wings increases with a change in sweep angle and a forward swept wing has positive sweep angle (Λ).

A. Static Tip Load Optimisations

Figure 4 and Figure 5 show the tip displacement and twist of all valid designs tried during six displacement maximisation and six twist maximisation optimisations when using the spars planform geometry has decision variables with "fixed end points" and "free end points" respectively. Additionally, the geometry of the structure and flexural axis for different designs are shown.

When considering the results obtained with "fixed end points", shown on Figure 4, it is clear that the variation in the spars shape changes the amount of tip displacement and tip twist seen by the wings by up to 6.9% and 0.69°. When considering the optimised designs obtained using "free end points", shown on Figure 5, the variation in the spars shape and root/tip location changes the tip displacement and tip twist by up to 7.5% and 0.72°. The use of curved spars and the spars root/tip location to increase the tip displacement and twist can be primarily related to a change in two geometric features: (1) the overall chord wise location of the spars with respect to the load application point and (2) the minimum chord wise distance separating the leading and trailing edge spar.

The overall chord wise location of the spars can be used to change the tip twist and the tip displacement of the wing as shown by Design 5 and 7 on Figure 4. In those designs the control of the spars shape has for primary effect

to move the spars towards the wing trailing and leading edge respectively. Design 5 and 7 have a tip flexural centre that has moved towards the trailing and leading edge respectively. The motion of the flexural axis implies that these wings would experience a higher nose-up/nose-down tip twist under a tip load pulling the wing out of the page (0.2^o and -0.19^o respectively). Hence the spars shape can create bend-twist coupling. This bend-twist coupling is due to an offset of the bending stiffness of the wing with respect to the load application point which results in a bending and torque load under a mid-chord tip load. This behaviour is similar to the bend-twist coupling created in swept wings and explains the increase in wing tip displacement (0.8% and 0.7% respectively). This similarity in bend-twist coupling mechanism can be observed on Figure 4 where the trend described by the variation in tip twist versus tip displacement for wings of different sweep angle and spars shape is seen to be similar. However since the load application does not move when using curved spars, wings with spars curved towards the leading edge (Design 7) or trailing edge (Design 5) develop negative/positive tip twist similarly to a wing swept backward/forward by 5^o.

The second geometric feature used is the minimum chord wise distance separating the leading and trailing edge spars which is found to reduce between Designs 3 and 4 on Figure 4 and leads to a reduction in the torsional constant of the wings. Additionally this geometric feature has a small effect on the wing bending stiffness by changing the support of the spars to the covers as shown by Designs 3, 4 and 6 on Figure 4.

However to get the maximum displacement and twist the combination of both geometric features is necessary as shown in Designs 1 to 4 and 8 to 11 on Figure 4. Indeed, wings with simple reduction in the chord wise distance between the spars similar to Designs 1 or 11 but made symmetric by the mid chord line so that the spars shape resemble a "dogbone" specimen have no twist and only a 1.0% increase in tip displacement. Designs 4 to 1 and 8 to 11 are the designs maximising twist for the least amount of tip displacement. The evolution of the spars shape from Designs 5 to 1 and 7 to 11 illustrates the use of the different geometric features by the optimiser. Initially, the chord wise distance separating the leading and trailing edge spar is reduced to a minimum (Designs 5 to 4 and 7 to 8). Then the minimum spar separation distance is moved towards the wing trailing or leading edge which leads to an offset in the flexural axis of the wing which creates bend-twist coupling when applying a tip load (Designs 4 to 2 and 8 to 10). Such offset implies that under a tip load the wings are subjected to a bending and torque load in addition to bend-twist coupling and so higher twist and displacement. Finally, the span location of the minimum distance between the spars is brought towards the root (Designs 2 to 1 and 10 to 11) which leads to higher displacement and twist since the bend-twist coupling and lower torsional stiffness occurs at higher loads. Based on these designs rules we summarise that the spar shape maximising the tip displacement and tip twist resembles Design 1 and 11.

An alternative to the "dogbone" no-twist design is the doubly curved spars of Design 12 on Figure 4 which leads to an increased in tip displacement of 7.8% and no twist as the bend-twist coupling created by the motion of the spars towards the leading edge in the first half of the wing span is neutralised by the bend twist coupling created by the motion of the spars towards the trailing edge in the second half of the wing span. However the increase in tip displacement due to the bend-twist coupling is maintained. The complexity of such designs which requires the movement of the control points of the spars in opposite direction was never pursued to its optimum by the optimiser.

When considering the optimised designs obtained using "free end points", shown on Figure 5, the two geometric features are similar to the one used on the optimised designs obtained with "fixed end points" and they are again used together to maximise variation to the tip displacement and twist however they are mainly controlled by the chord wise location of the spars root and tip instead of the spars shape. For example, when considering the evolution of the spar design from Design 8 to 11 it can be seen that the second geometric feature is achieved over all of the span length first and then the spars are moved towards the leading edge. However the spars are mainly straight and it is the chord wise location of the spars root and tip that improves the design. Using such design rules, the design generating the highest tip displacement and nose-down twist can be simplified as the one shown on Figure 6. This design increases tip displacement and twist by 10.3% and -0.93^o respectively. Thus the control of the spars root and tip location increases tip twist and displacement by up to 34.8% and 3.3% compare to changing only the spars shape.

The use of the spars root and tip chord wise location is also found to change the wing deformation by placing the spars at an angle to the wing span direction as shown by Designs 6, 7 and 12 similarly to a change in wing sweep. Interestingly, Design 12 has no twist but a tip displacement increased by 1.7%. This result can be explained by the fact that the spars run diagonally from the root trailing edge corner to the tip leading edge corner hence any twist due to the bend-twist coupling in the first half of the wing is neutralised by the twist created in the second half.

The combination of both geometric features when changing the spars geometry is a key difference with the effect of changing the wing sweep as the torsional constant of the wing is almost unchanged by the spar sweep angle as shown in [31]. Additionally, changing the spar sweep leads to higher bending loads has the load is carried over a longer distance which leads to higher tip displacement. These differences in effect imply that the spars geometry has higher control on the tip twist than the sweep angle hence to match the tip twist of Designs 1 and 11 on Figure 4 and Figure 5 a sweep angle superior to 15^o is needed.

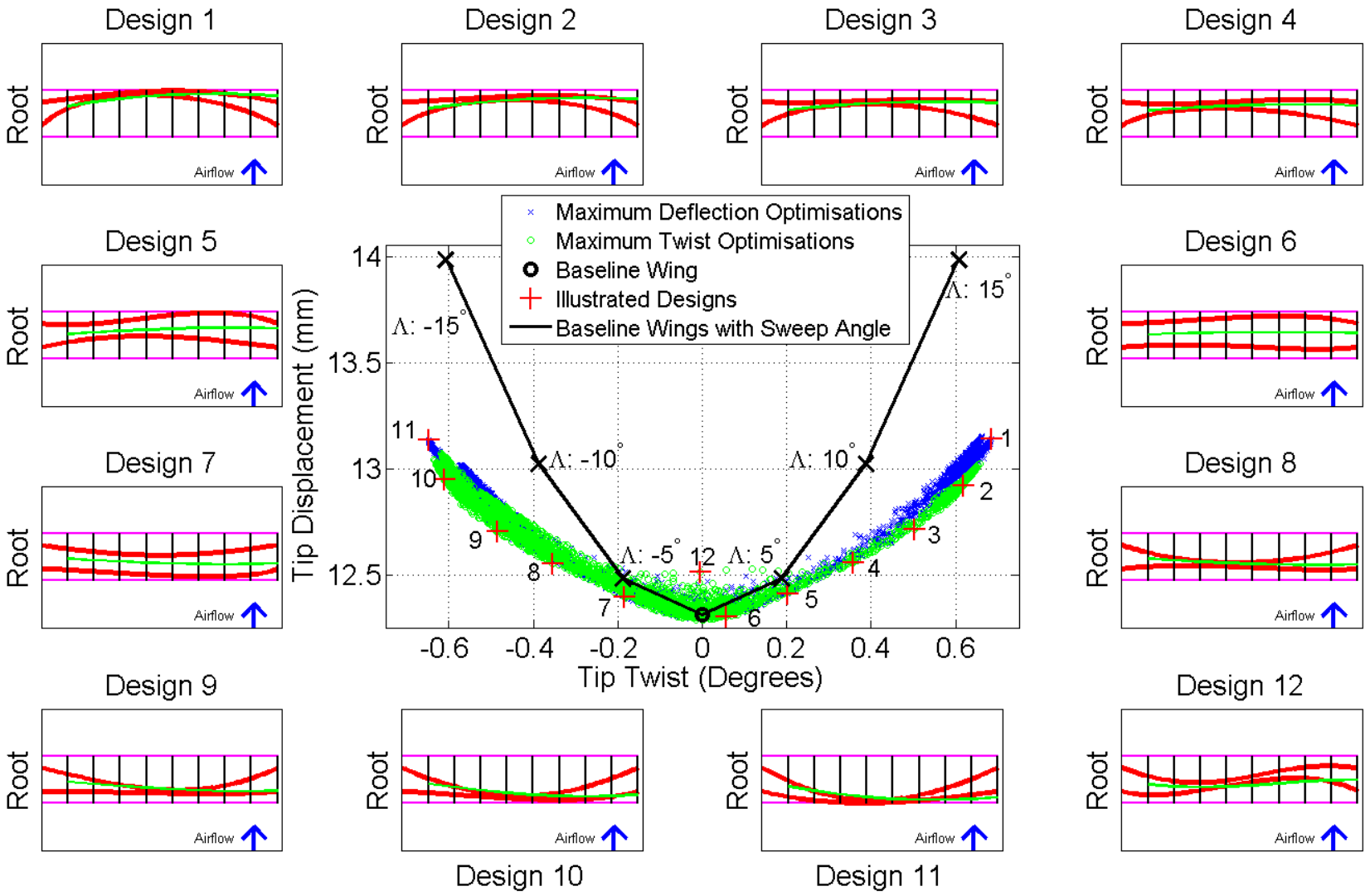

Figure 4. Tip Displacement versus Tip Twist for all Valid Spars Designs with "Fixed End Points" under a Tip Load and Illustration of Spars Designs. The Tip Displacement and Twist for Wings with Different Sweep Angle (Λ) with a 5° increment are also shown.

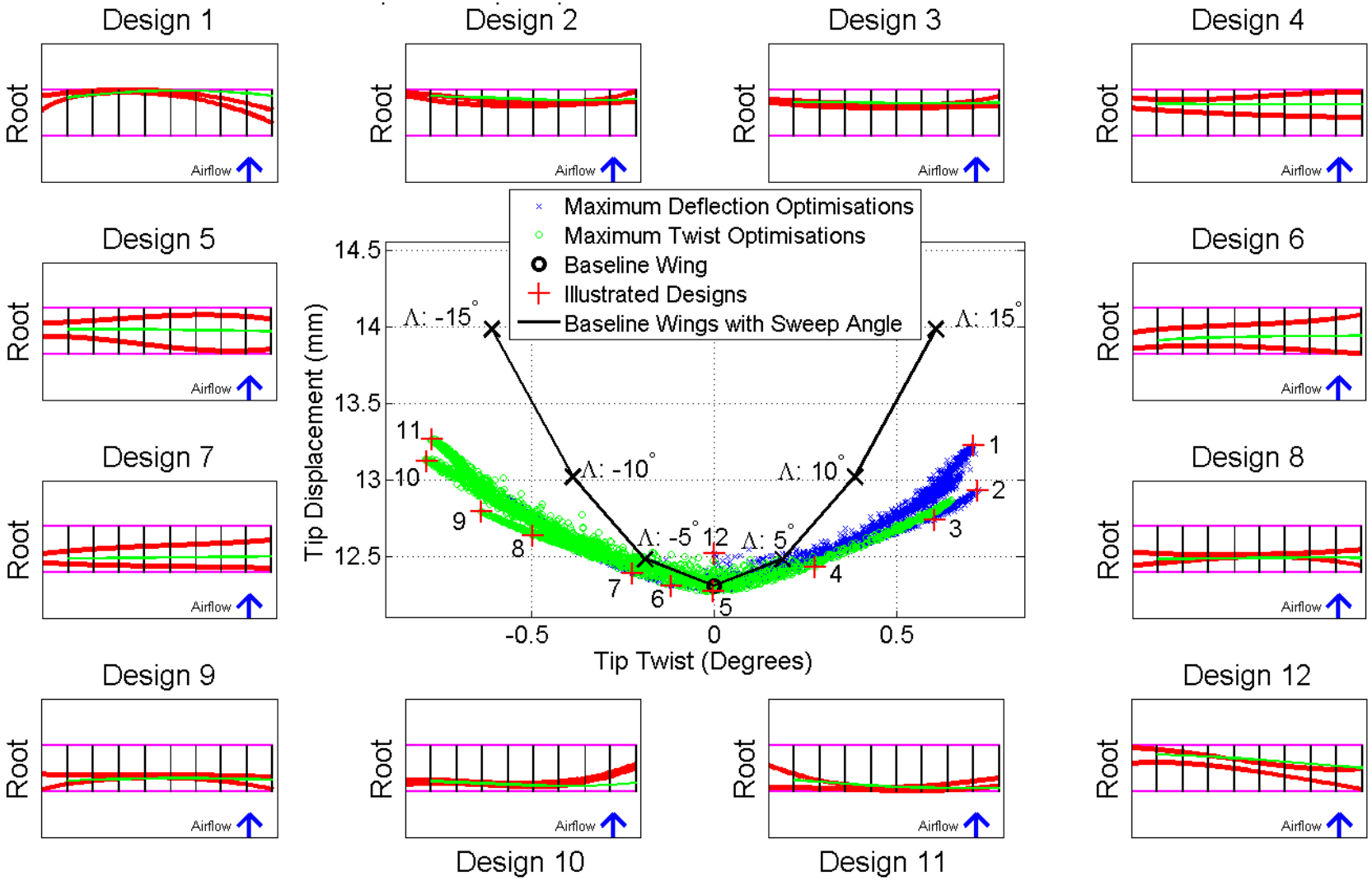

Figure 5. Tip Displacement versus Tip Twist for all Valid Spars Designs with "Free End Points" under a Tip Load and Illustration of Spars Designs. The Tip Displacement and Twist for Wings with Different Sweep Angle (Λ) with a 5° increment are also shown.

Figure 6. Spars Design Maximising Nose-Down Tip Twist and Displacement under a Static Tip Load found following the Design Rules Extracted from the Optimisations Results.

B. Natural Frequency Optimisations

Figure 7 shows the normalised natural frequencies for each of the first eight mode of every valid designs tried during twelve different optimisations with "fixed end points". Figure 7 also shows the normalised natural frequencies for the first eight bending and torsion modes of wings swept backward by 5° and 30° taken from [31]. The natural frequencies have been normalised with the Baseline natural frequencies and only bending and torsion modes are considered in this analysis. Figure 8 represents the same data set except that the natural frequencies are not normalised and the natural frequency of mode *n* is plotted against the natural frequency of mode *n+1* hence Figure 8 contains six different plots (variation of mode 2 with respect to mode 1 is not represented). Each optimisation data set is split into two categories: (1) wing designs with similar mode succession as the Baseline wing and (2) wing designs with a mode succession different than the Baseline wing. Hence mode 1 to 8 for the wings with a similar mode succession as the Baseline wing are: first bending, second bending, first torsion, third bending, second torsion, fourth bending, third torsion and fifth bending mode. Wings with a different mode succession represent 3.6% of all valid designs tried but they always have their first bending mode has mode 1 and mainly have mode swaps due to lower torsion modes natural frequency. Finally the numbers on Figure 7 and Figure 8 refer to the illustrated designs shown on Figure 9. The illustrated designs maximise a natural frequency variation with the Baseline wing value for at least one mode. Designs 1 to 10 have a similar mode succession as the Baseline wing while Design 11 and 12 have a different mode succession.

Similarly the data for twelve optimisations when using "free end points" is presented on Figure 10-12. Wings with a different mode succession than the Baseline wing represent 20.4% of all valid designs tried. Designs 1 to 8 on Figure 10-12 have similar mode succession as the Baseline wing while Design 9 to 15 do not.

The first observation that can be made on Figure 7 and Figure 10 is that changing the spars geometry has very little effect on the first bending mode of the wing. The natural frequency of the first bending mode varies by at most 0.2Hz on Figure 7 and 0.5Hz on Figure 10 with a change in spars geometry. Hence the first bending mode natural frequency is very weakly dependent on the geometry of the spars. However as the mode number increases the dependency of the natural frequencies on the spars geometry increases as the dependency of their natural frequency on the wing stiffness and its distribution increases. Maximum dependency is found for the third torsion mode (Mode 7) for which a change in the spars geometry can lead to a variation of 111.0Hz and 126.2Hz on Figure 7 and Figure 10 respectively when considering only the wings with similar mode succession as the Baseline wing.

When considering Figure 8 and Figure 11 it can be seen that the wings maximising the natural frequency of each mode (upper right quadrant for each plot) are primarily wings with similar mode succession as the Baseline wing. The only exception to this trend is Design 9 and 10 on Figure 10-12 for which the fifth bending and the third torsion modes are swapped. However it should be noted that Design 9 and 10 are very similar to Design 2 on Figure 12. On the other hand the majority of wings with different mode succession than the Baseline wing are found to enable natural frequency minimisation (bottom left quadrant of each plot).

When considering only the wings with the same mode succession as the Baseline wing we observed that the variation in natural frequencies with the spars shape for the torsion modes (Modes 3, 5 and 7) is found to be superior than the one observed for the bending modes natural frequencies (Modes 2, 4, 6 and 8) as shown on Figure 7-9 and Figure 10-12. The natural frequencies of the bending modes are only marginally increased compared to the Baseline values by up to 1.5% and 1.6% on the fifth bending mode but can be drastically decreased by reducing the chord wise

distance separating the spars by up to 17.0% and 21.1% on the same mode. The torsion modes natural frequencies can be drastically both increased (by up to 17.0% and 19.9%, third torsion mode) and reduced (by up to 13.2% and 14.5%, third torsion mode) by changing the chord wise distance separating the spars. Hence the torsion modes natural frequencies are more dependent on the spars geometry than the bending modes.

As explained in [31] and shown on Figure 7 and Figure 10, changing the sweep angle mainly reduced the bending mode natural frequencies as the wing mass increases. When increasing the sweep angle from 0^{o} to 30^{o} the fifth bending mode and fourth torsion mode natural frequencies are reduced by 18.1% and 0.9% respectively. Thus changing the spars geometry offers a much higher control over the wing natural frequencies than changing the wing sweep.

When considering the results obtained with "fixed end points", the bending modes natural frequencies are maximised by Designs 1, 3 and 5 on Figure 9 while Designs 2, 4 and 6 maximise the natural frequencies of the torsional modes. All display curved spars for which the leading and trailing edge spars are symmetric by the mid-chord line. In all these designs, curved spars are used to increase the chord wise distance separating the spars however this distance is significantly more increase on Designs 2, 4 and 6 than on Designs 1, 3 and 5. Interestingly Designs 1, 3 and 5 have increased torsion mode natural frequencies while Designs 2, 4 and 6 have reduced bending mode natural frequencies compared to the Baseline wing.

A similar distinction is seen on Figure 12 where Designs 1 and 3 have the highest bending mode natural frequencies and increased torsional mode natural frequencies due to a slight increase in the chord wise distance separating the spars. Designs 2, 4, 5, 9 and 10 have the highest torsional mode natural frequencies but reduced bending mode natural frequencies. These designs display a significant increase in the chord wise separation of the spars. Although Designs 9 and 10 have a different mode succession than the Baseline wing they can be used in this explanation as the only difference in their mode succession to the Baseline is a swap between the fifth bending (436.0Hz and 443.9Hz) and third torsion mode (423.5Hz and 415.2Hz). Hence the trend displayed on Figure 10 would be increased if a mode reordering was performed for Design 9 and 10.

Table 4 and Table 5 show the tip twist and displacement for the designs shown on Figure 9 and Figure 12 when under a tip load similar to the load used in Section IV.A. Clearly Design 1, 3 and 5 on Figure 9 and Designs 1 and 3 on Figure 12 have a lower tip displacement than the Baseline wing which would translate into a higher bending stiffness and so a higher bending mode natural frequencies. On the other hand Design 2, 4 and 6 on Figure 9 and Designs 2, 4, 5, 9 and 10 on Figure 12 have a higher tip displacement than the Baseline wing which imply a lower bending stiffness and so a lower bending mode natural frequencies. Hence the effect of increasing the chord wise distance separating the leading and trailing edge spars on the wing bending stiffness varies based on that distance.

Hence in both decision variables set it is clear that the optimiser uses the chord wise distance separating the leading and trailing edge spar to maximise the modes natural frequencies which primarily change the torsional constant of the wing. The change in wing bending stiffness is a much smaller effect as it is related to the support of the skins by the spars. This hierarchy in the stiffness variation mechanism explains why the maximisation of the bending mode natural frequencies is smaller than the maximisation of the torsion modes natural frequencies.

When the root and tip location of the spars is fixed these geometric features are controlled by a change in spar shape however when the spars root and tip position are decision variables they are used in conjunction with predominantly straight spars.

Figure 7 and Figure 10 display many designs that lead to drastic reduction in mode natural frequencies. Designs with the lowest natural frequencies display a reduction in chord wise separation of the spars (Designs 7-12 on Figure 9 and Designs 6- 8 ,11, 13, 14 and 15 on Figure 12) and/or spars with chord wise overall position towards the leading or trailing edge (Designs 7, 9, 11 and 12 on Figure 9 and Designs 6, 7, 12, 15 on Figure 12) and/or asymmetric leading and trailing edge shapes spars by the mid chord line (Designs 7, 9 and 11 on Figure 9 and Designs 6, 7, 8, 12 and 15 on Figure 12). Such geometric features have for primary effect to reduce the torsional constant of the wing as well as create bend-twist coupling as shown in Section IV.A, Table 4 and Table 5. This coupling enable further changes in the natural frequency for the different modes. These results highlight the control of the wing modal response with the spars shape and the spars root/tip chord wise location.

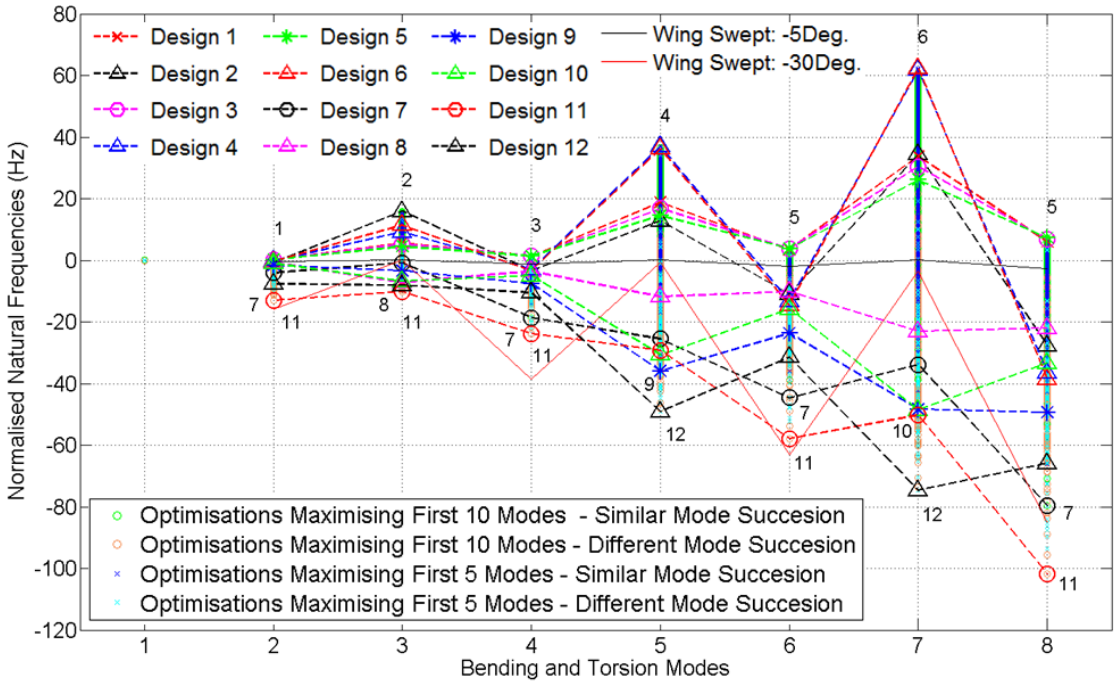

Figure 7. Normalised Natural Frequencies of the First Eight Modes of all Valid Spars Designs with "fixed end points". The Numbers Refer to the Designs shown on Figure 9. The Normalised Natural Frequencies for the First Eight Bending and Torsion Modes of Wings Swept Backward by 5° and 30° are also shown.

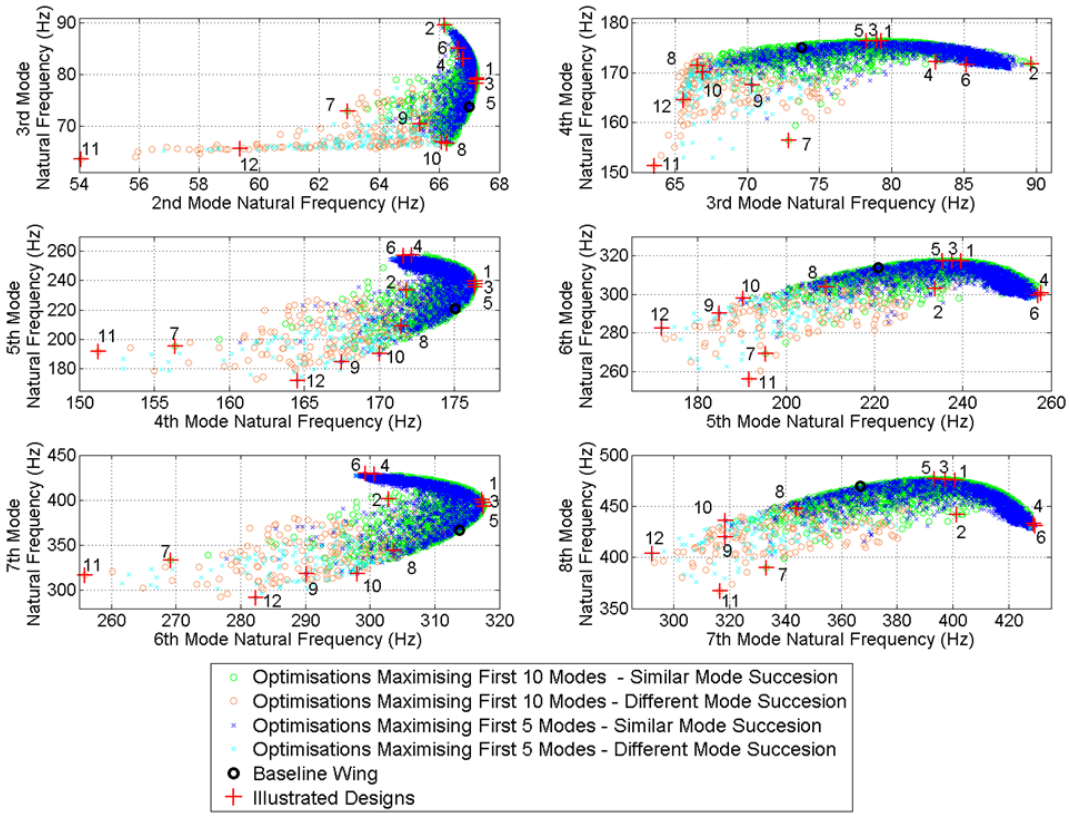

Figure 8. Natural Frequencies Variation for Mode 2 to 8 of all Valid Spars Designs with "fixed end points". The Numbers Refer to the Designs shown on Figure 9.

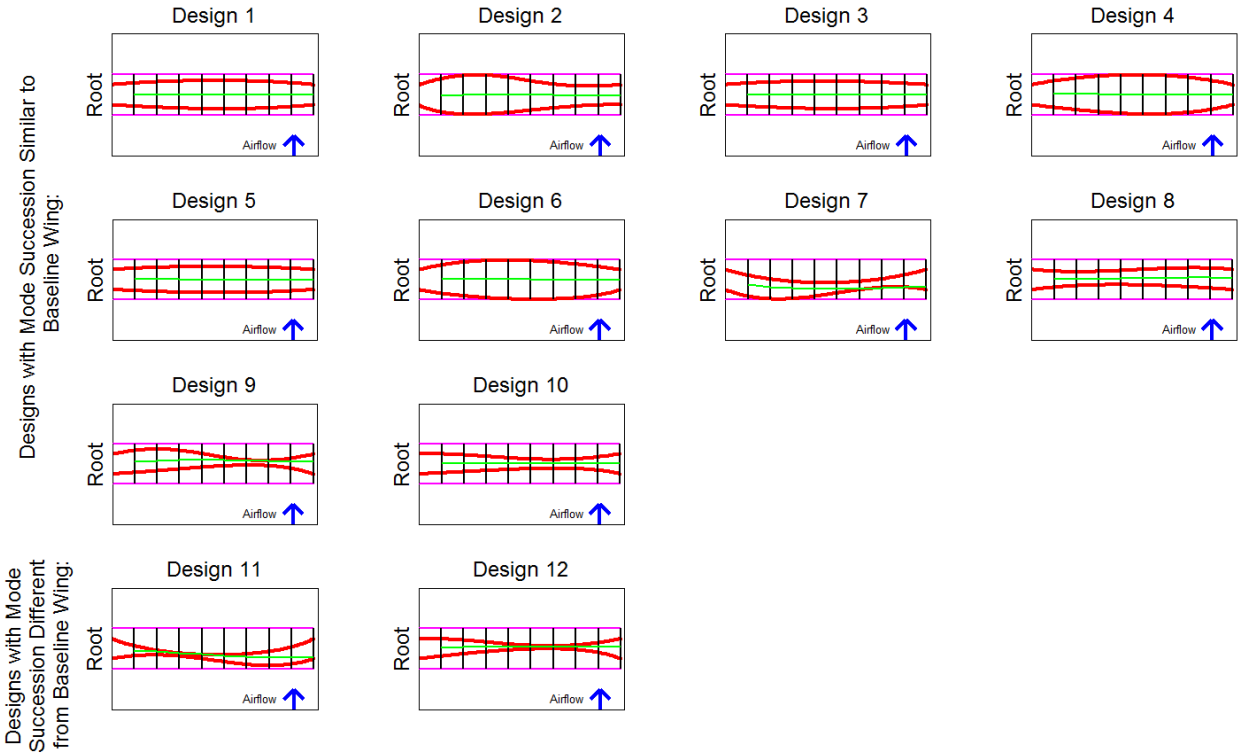

Figure 9. The Spar Designs with "Fixed End Points" Maximising Variation with the Baseline Values of each Mode.

Table 4. Tip Displacement and Twist of the Designs shown on Figure 9 when Subject to a Mid-Chord Tip Load.

	Designs	Average Tip Displacement (mm)	Tip Twist (Degrees)
Figure 9	1	12.30	0.00
	2	12.40	-0.01
	3	12.30	0.00
	4	12.33	0.00
	5	12.30	0.00
	6	12.34	-0.01
	7	12.55	-0.27
	8	12.34	0.07
	9	12.42	0.10
	10	12.37	0.01
	11	12.64	-0.43
	12	12.43	0.09

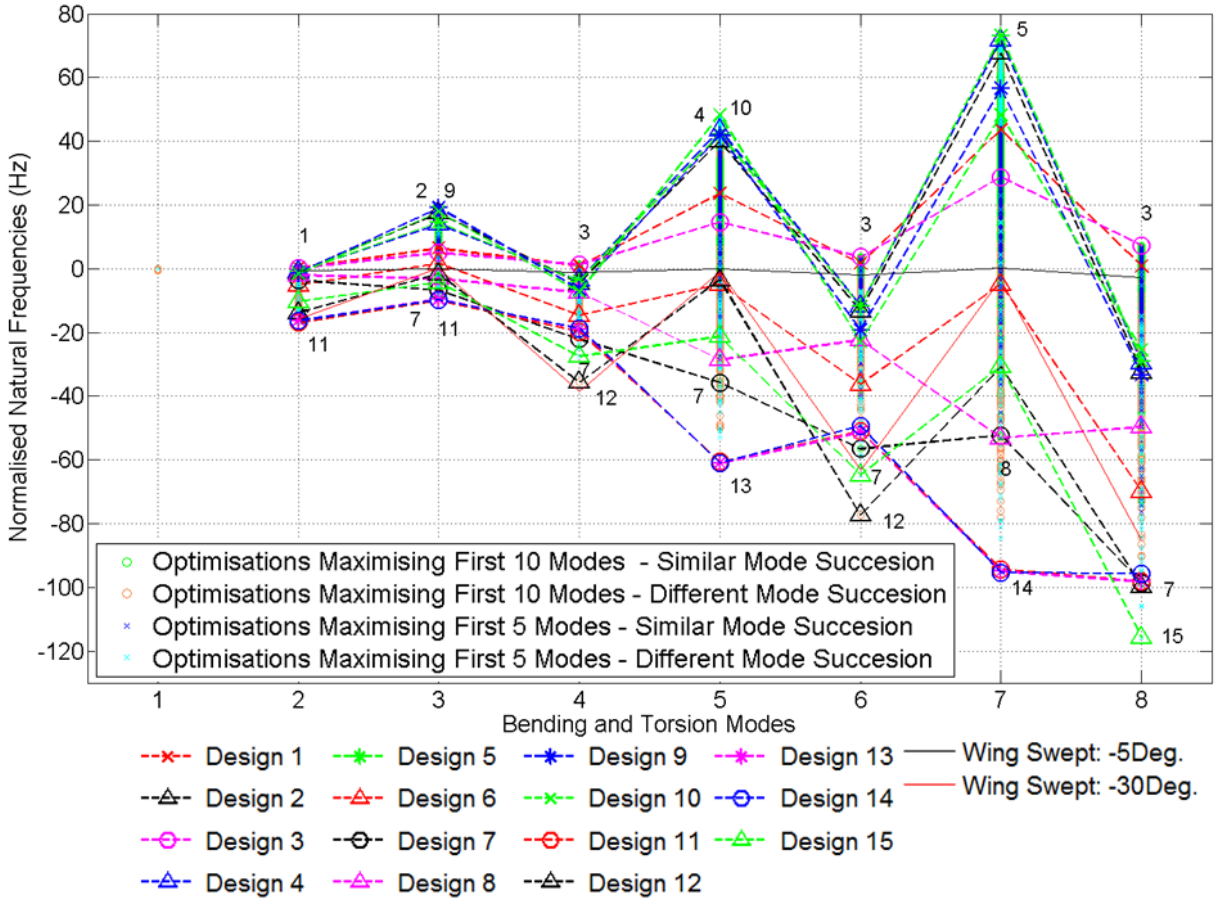

Figure 10. Normalised Natural Frequencies for the First Eight Modes of all Valid Spars Designs with "Free End Points". The Numbers Refer to the Designs shown on Figure 12. The Normalised Natural Frequencies for the First Eight Bending and Torsion Modes of Wings Swept Backward by 5° and 30° are also shown.

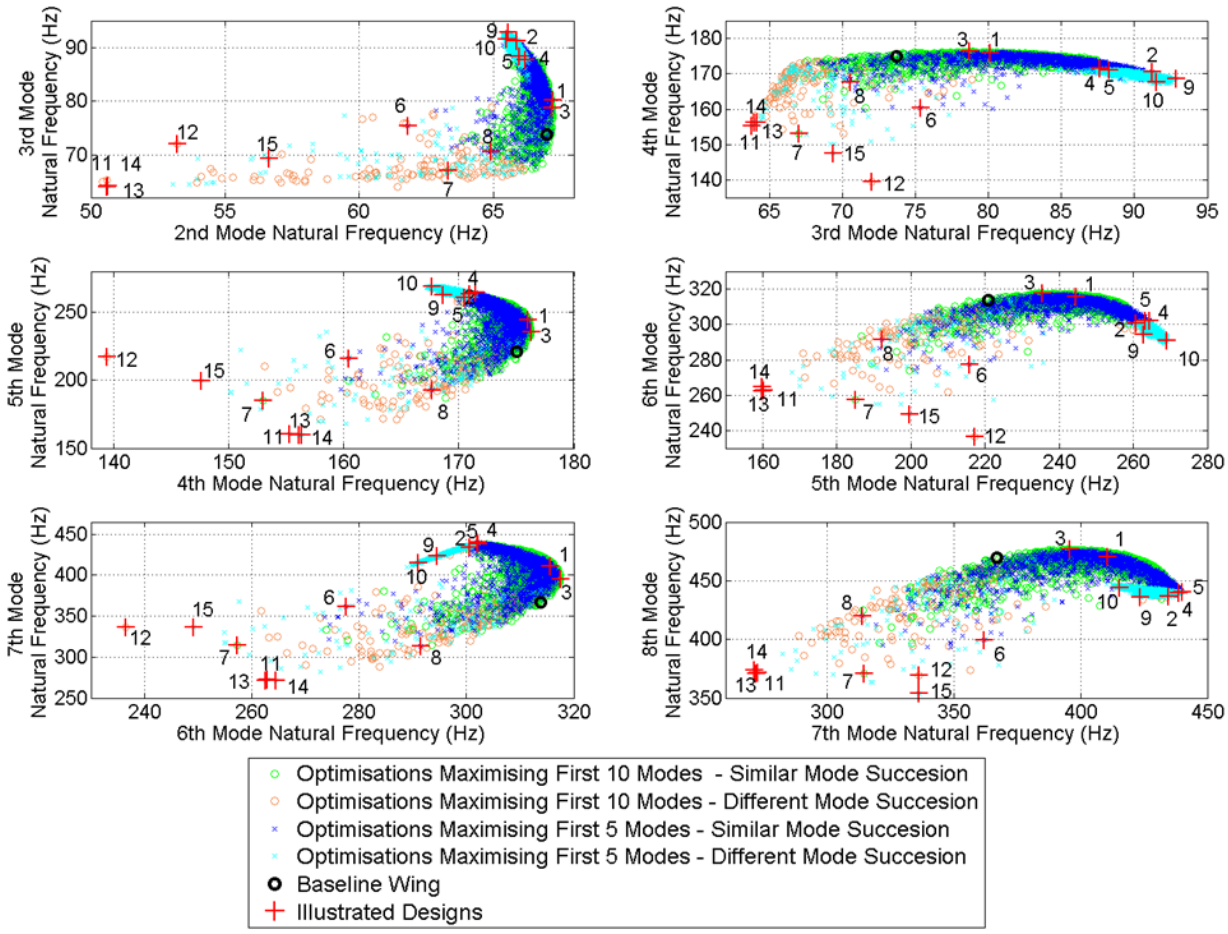

Figure 11. Natural Frequencies Variation for Mode 2 to 8 of all Valid Spars Designs with "Free End Points". The Numbers refer to the Designs shown on Figure 12.

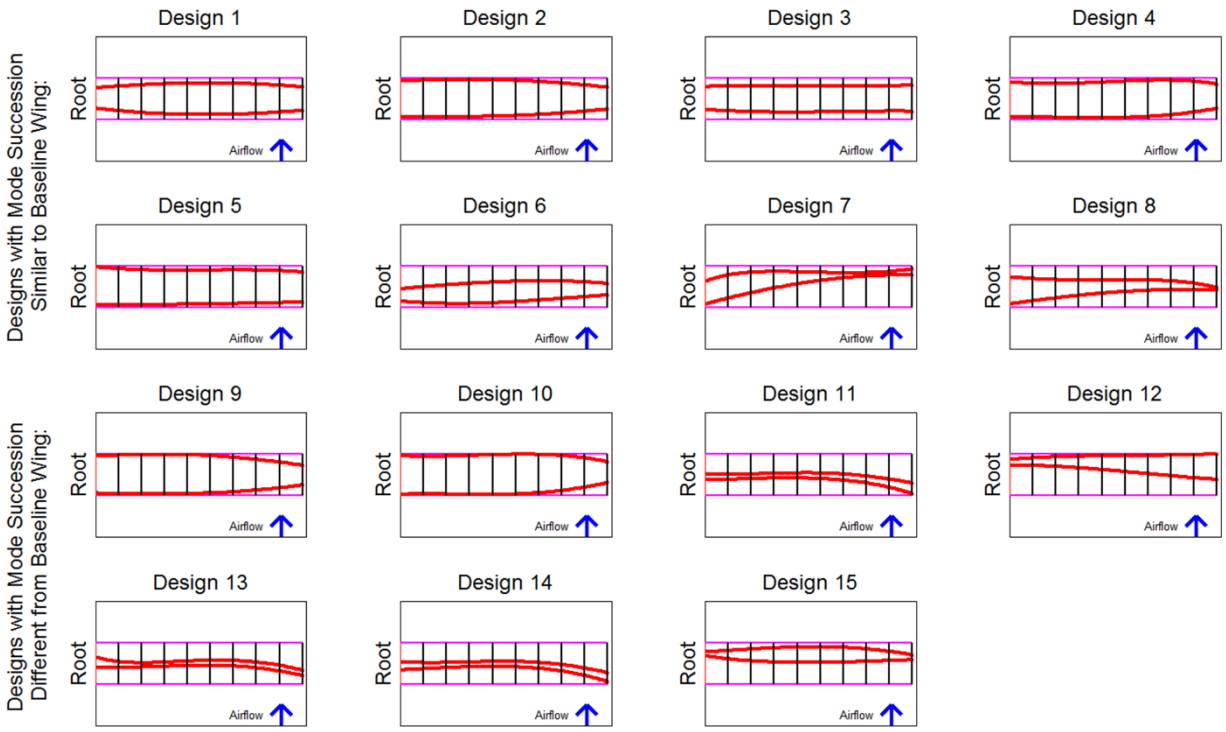

Figure 12. The Spar Designs with "Free End Points" Maximising Variation with the Baseline Values of each Mode.

Table 5. Tip Displacement and Twist of the Designs shown on Figure 12 when Subject to a Mid-Chord Tip Load.

	Designs	Average Tip Displacement (mm)	Tip Twist (Degrees)
Figure 12	1	12.30	-0.01
	2	12.37	0.01
	3	12.30	-0.01
	4	12.35	0.01
	5	12.35	-0.01
	6	12.40	-0.18
	7	12.79	0.52
	8	12.43	0.00
	9	12.39	-0.01
	10	12.39	0.02
	11	12.52	-0.29
	12	12.65	0.43
	13	12.48	-0.16
	14	12.51	-0.27
	15	12.59	0.40

C. Static Aeroelastic Optimisations

Figure 13 and Figure 16 show the tip displacement versus tip twist for all valid designs tried when changing the spars geometry with "fixed end points" and "free end points" respectively. Additionally, the wing structure geometry and flexural axis for different designs are shown including Designs 1 to 11 on Figure 13 and Designs 1 to 10 on Figure 16 are designs maximising tip twist for minimum tip displacement.

Changing the spars shape can enable a 39.6% and 363.5% increase in tip displacement and twist and 6.6% and 164.9% decrease in tip displacement and twist under aerodynamic loading compared to the Baseline wing when using "fixed end points". Similarly changing the spars shape and root/tip spar location can lead to a 59.2% and 536.0%

increase in tip displacement and tip twist and 8.0% and 173.0% decrease in tip displacement and twist under aerodynamic loading compared to the Baseline wing. It is interesting to notice that the designs with minimum tip twist and displacement have a tip twist approximating to the tip displacement and twist of a wing swept back by 20° while Designs maximising tip twist and displacement have tip twist close to a wing swept forward by at least 30°. Hence changing the spars shape and/or root and tip spar location can drastically vary the tip displacement and twist.

Designs maximising the tip displacement and twist (Designs 1, 2 and 3 on Figure 13 and Designs 1 to 5 on Figure 16) display a reduction in the distance separating the spars and the spars minimum distance is located towards the trailing edge of the wing. The designs minimising tip displacement and twist (Designs 10 and 11 on Figure 13 and Designs 9 and 10 on Figure 16) have their spars located towards the leading edge of the wing and display a reduction in the distance separating the spars. Hence the wing deformation is changed due to a variation in two geometric features: (1) the overall chord wise location of the spars with respect to the mid-chord line and (2) the minimum chord wise distance separating the leading and trailing edge spar.

The overall chord wise location of the spars is clearly used to influence the bend-twist coupling behaviour of the wing. Wings with tip twist higher than the Baseline wing (Designs 1, 2, 3 and 4 on Figure 13 and Designs 1 to 5, 11 and 12 on Figure 16) have their spars towards the leading edge hence increasing the distance between the region where most of the load is applied (around the quarter chord line) and the flexural axis. On the other hand the wings with a lower tip twist than the Baseline wing (Designs 8, 9, 10 and 11 on Figure 13 and Designs 7 to 10 on Figure 16) have their spars towards the leading edge hence minimising the distance between the load application region and the flexural axis.

The effect of the minimum chord wise distance separating the spars can be associated to a reduction in the torsional stiffness of the wing box which enable the wing to twist more under a bending load. This behaviour explains how Designs 4, 5 and 6 on Figure 13 and Design 6 on Figure 16 have increased tip displacement and twist. Additionally, this geometric feature has been shown to increase the bending deformation of the wing in Section IV.A. Hence for wings with a negative tip twist the reduction in the chord wise spar separation has conflicting effects of increasing the torsional and bending stiffness. This conflicting effects on the wing deformation explains the change in the tip displacement - twist relationship from linear to non-linear as shown on Figure 13 and Figure 16.

Although similar geometric features are used by the different decision variable sets these geometric features are changed by using curved spars in the “fixed end points” optimisation and changed mainly by moving the spars root and tip chord wise location in the “free end points” optimisations. Indeed, when the root and tip chord wise location of the spars are freed to move the spars are mainly straight. Hence the root and tip chord wise location of the spars has a slightly higher effect on the tip twist and displacement than curved spars. The idealised designs presented in Figure 6 maximising tip twist and displacement under a tip load would also lead to the highest tip twist reduction of 218.7%.

Figure 14 and Figure 17 show the twist distribution along the span for the designs shown on Figure 13 and Figure 16 respectively. The twist distribution for the wings with a sweep angle of -20° and 30° are also displayed. Controlling the spars shape and root/tip spar location enable significant variations in tip twist magnitude and sign as well as twist distribution along the span. For example, the twist distribution is changed from an almost elliptic variation for Design 1 to an almost linear variation in Design 9 on Figure 14. This variation in twist distribution is close to variation in twist distribution observed by changing the wing sweep angle from 30° forward to 20° backward. This result highlight the potential of the spars shape and root/tip spar location to control aeroelastic problems such as flutter/divergence and stall tendency.

Finally, the effect of changing the spars shape and root/tip spar location on the root bending moment of the wing is shown on Figure 15 and Figure 18 with “fixed end points” and “free end points” respectively. The root bending moment is found to be linearly proportional to the tip twist of the wing hence wings with maximum/minimum tip twist and displacement also have maximum/minimum root bending moment as a reduction in the tip twist enables a reduction in the angle of attack at each section along the wing hence lesser lifting force. The root bending moment can be reduced by 11.3% and 12.8% compared to the Baseline wing when controlling the spars shape and root/tip chord wise location. To achieve a similar reduction in root bending moment with straight spars, the wing needs to be swept backward by 15-20°.

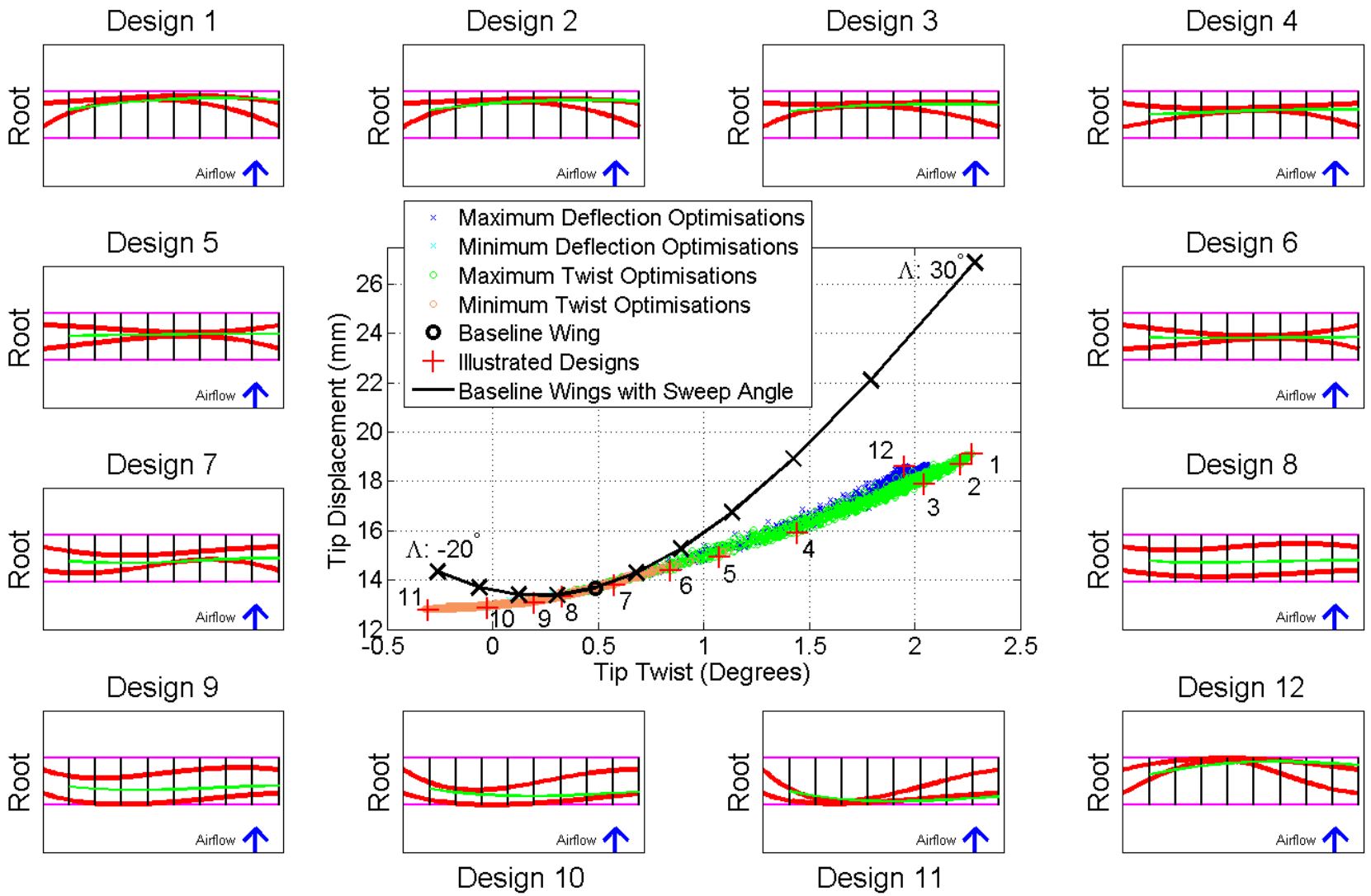

Figure 13. Tip Displacement versus Tip Twist for all Valid Spars Designs with "Fixed End Points" under Aerodynamic Loading and Illustration of Spars Designs. The Tip Displacement and Twist for Wings with Different Sweep Angle (Λ) with a 5° increment are also shown.

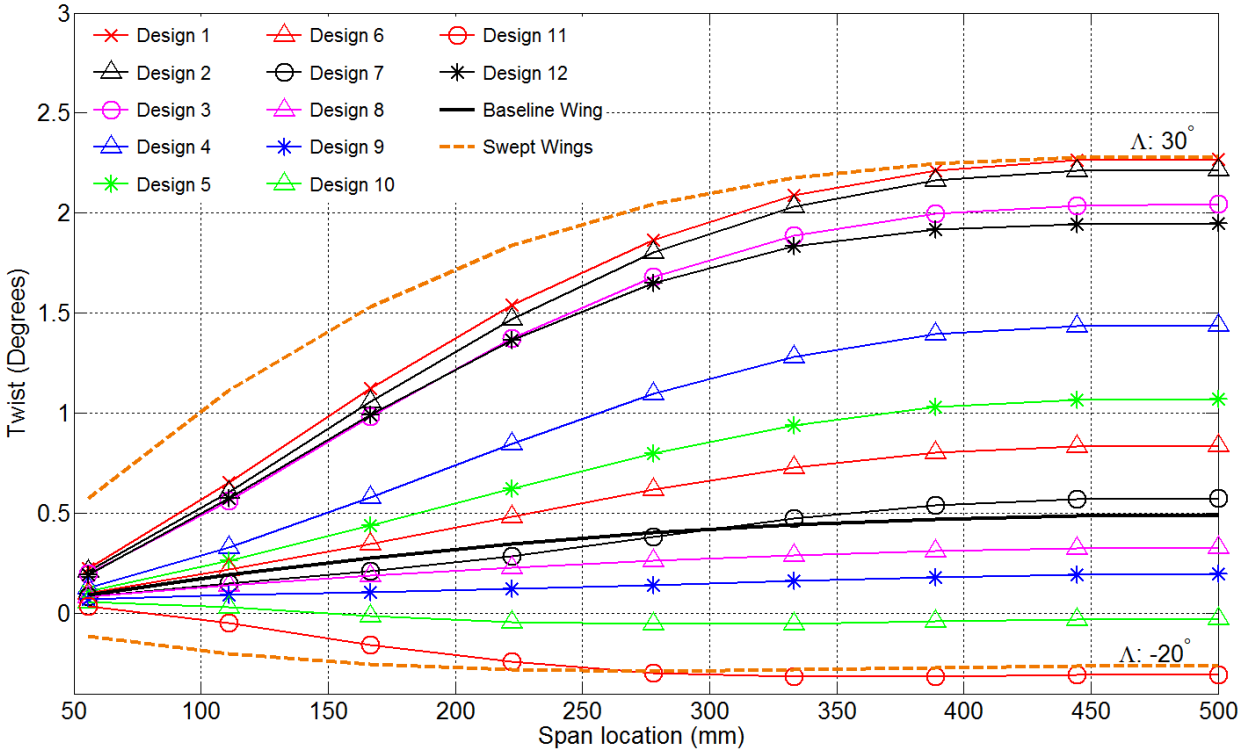

Figure 14. Twist along the Wing Span for the Designs shown on Figure 13 and Wings Swept by 30º and -20º.

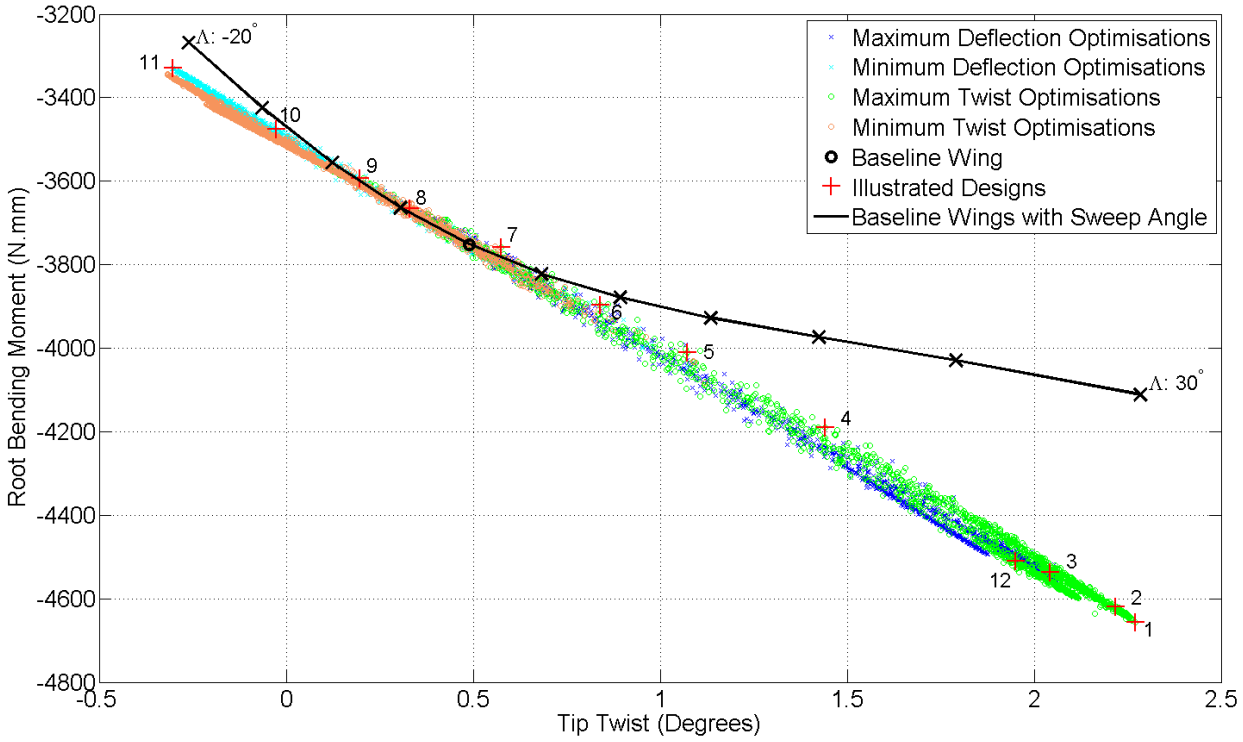

Figure 15. Root Bending Moment versus Tip Twist for all Valid Spars Designs with "Fixed End Points" and for Several Wings Swept under Aerodynamic Loading. The Designs are shown on Figure 13.

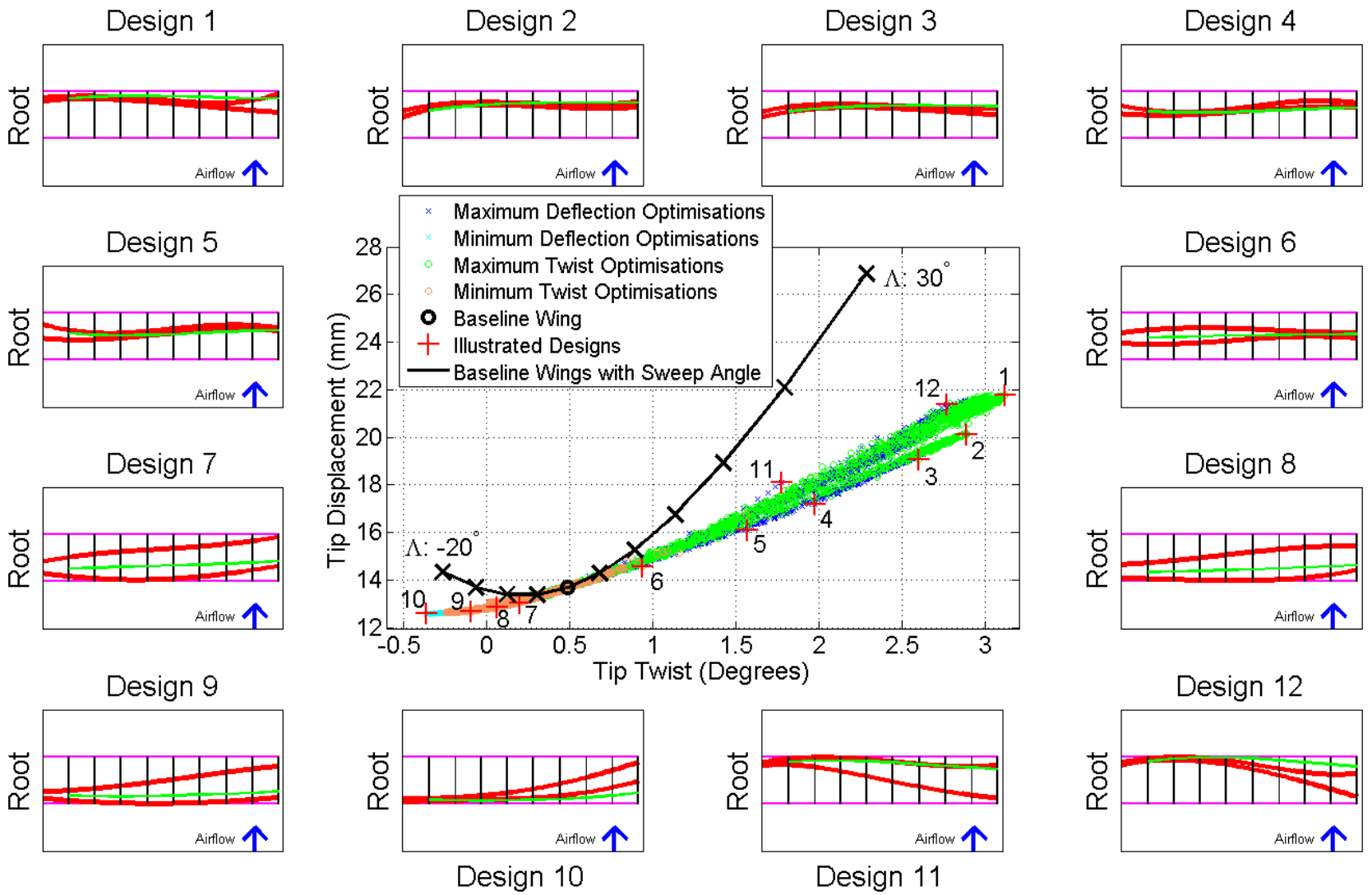

Figure 16. Tip Displacement versus Tip Twist for all Valid Spars Designs with "Free End Points" under Aerodynamic Loading and Illustration of Spars Designs. The Tip Displacement and Twist for Wings with Different Sweep Angle (Λ) with a 5° increment are also shown.

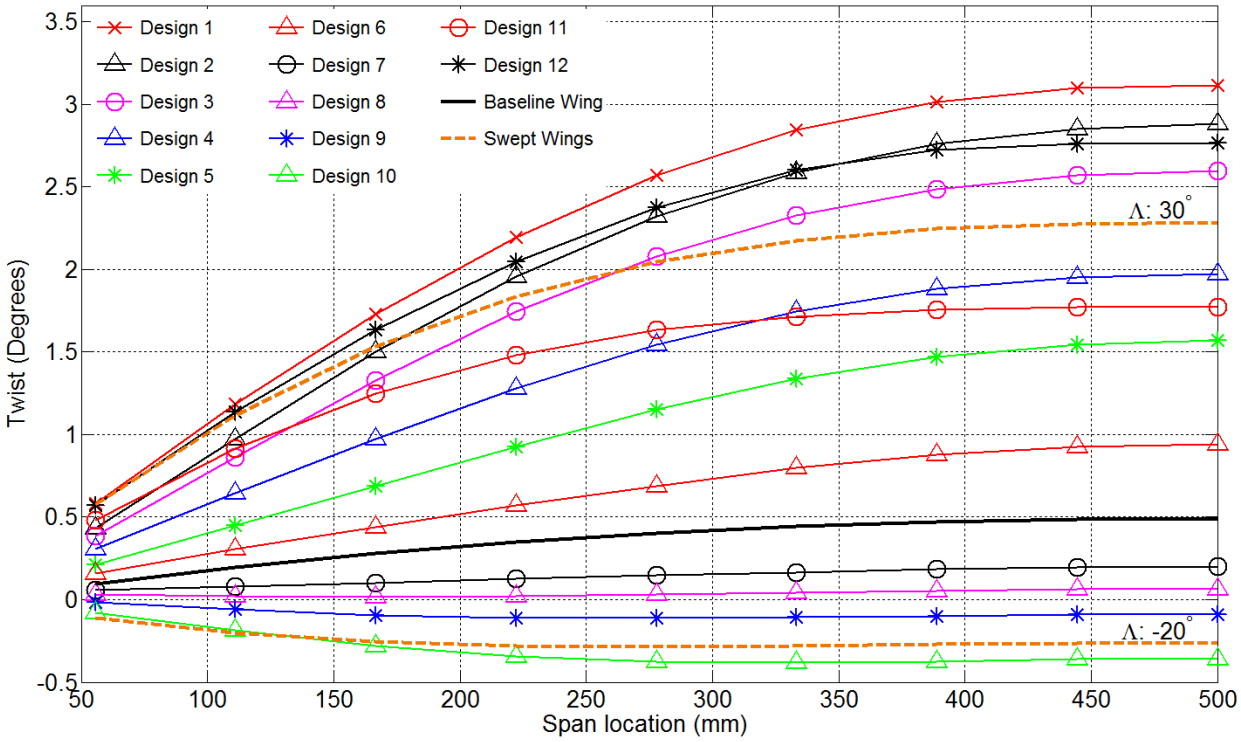

Figure 17. Twist along the Wing Span for the Designs shown on Figure 16 and Wings Swept by 30º and -20º.

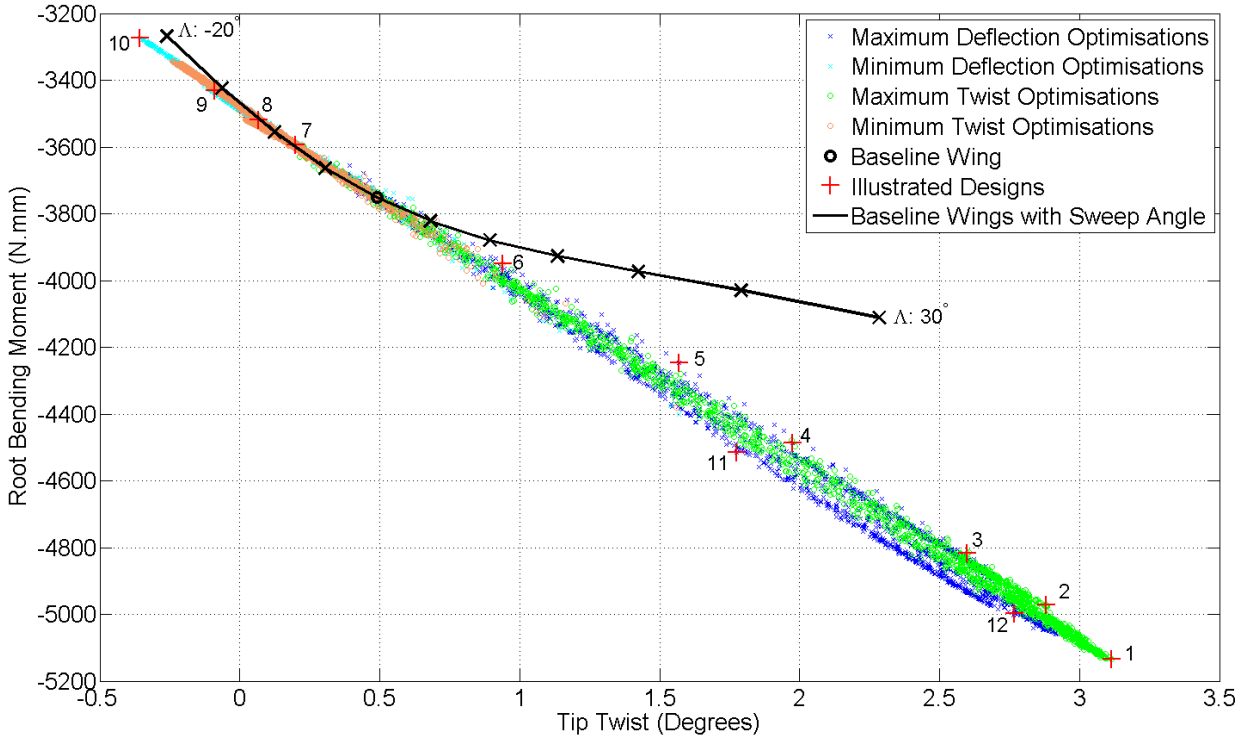

Figure 18. Root Bending Moment versus Tip Twist for all Valid Spars Designs with "Free End Points" and for Several Wings Swept under Aerodynamic Loading. The Designs are shown on Figure 16.

D. First Aeroelastic Instability Speed and Gusts Load Optimisations

Figure 19 and Figure 20 show the flutter/divergence speed versus maximum root bending moments experience during a worst case scenario gust event for all valid designs tried when changing the spars geometry with "fixed end points" and "free end points" respectively. Additionally, the wing structure geometry and flexural axis for different designs of interest are shown. The different wing designs are split by the nature of their aeroelastic instability. Wings suffering aeroelastic divergence are represented by a "△" symbol, wings suffering a hard flutter instability are represented by a "×" symbol and finally wings suffering a soft flutter instability are represented by a "+" symbol.

The flutter speed is found to be increased by up to 28.6% and 31.7% when changing the spars geometry using "fixed end points" and "free end points" respectively. This improvements in flutter speed are achieved by Designs 12 and 11 on Figure 19 and Figure 20, respectively, and are found to suffer a hard flutter similar to the Baseline wing due to the first bending mode, second bending mode and first torsion. Both Designs have increased the chord wise distance separating the spars compared to the Baseline wing and a flexural axis only marginally different than the Baseline wing. This geometric features are similar to the Designs found maximising torsional natural frequencies of the wing in Section IV.B. Hence the optimisation of the spars shape and/or root/tip chord wise location enables an increase in the wing natural frequencies (especially for the torsional modes) which lead to large increase in flutter speed which is un-match by a change in sweep angle.

The root bending moment during a worst case scenario gust encounter can be reduced by up to 11.1% and 6.0% when changing the spars geometry using "fixed end points" and "free end points" respectively as shown by Design 9 on Figure 19 and Design 8 on Figure 20. Both Designs have a flexural axis towards the leading edge of the wing implying that under an aerodynamic load there tendency to twist is reduced compared to the Baseline wing as explained in Section IV.C. Hence the creation of bend-twist coupling by changing the spars geometry enables a strong reduction in the root bending moment similar to sweeping the wing back by around 15^{o}.

However the creation of the bend-twist coupling by reducing the chord wise distance separating the spars and by offsetting the spars overall chord wise location lead to wings with reduced torsional stiffness and natural frequencies, as explained in Section IV.B and IV.C, leading to a reduction in the flutter speed of the wing (Design 9 on Figure 19 and Design 8 on Figure 20 have a flutter speed reduced by 13.5% and 25.4% respectively). Thus when considering designs leading to large improvements in flutter/divergence speed and the root bending moment during gust there is a clear trade-off between the geometry of the spars and the metric improved.

Design 11 on Figure 19 and Design 9 on Figure 20 have a flutter speed 6.1% and 20.7% higher and a maximum root bending moment 5.0% and 3.7% lower than the Baseline wing. Hence changing the spars geometry can lead to some improvements in both flutter/divergence speed and the root bending moment as shown by numerous designs. It should be noted that designs with small improvements in both metrics are also more viable for manufacturing as only small changes in spars geometry are performed.

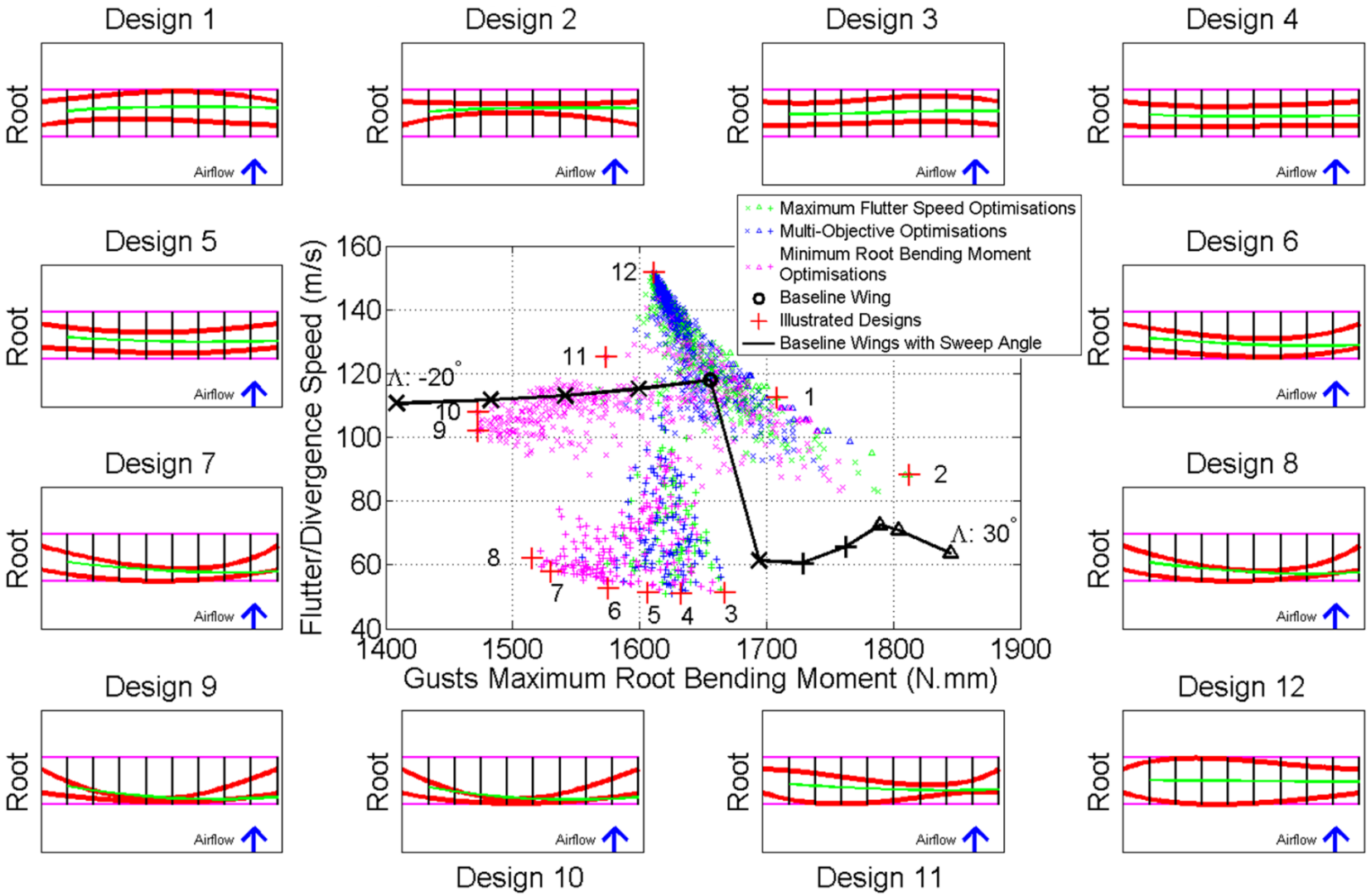

Figure 19. Flutter/Divergence Speed versus Maximum Root Bending Moment during a Worst Case Scenario Gust Event for all Valid Spars Designs with "Fixed End Points" and Illustration of Spars Designs. The Flutter/Divergence Speed and Root Bending Moment for Wings with Different Sweep Angle (Λ) with a 5° increment are also shown. Hard flutter is identified by a "×" symbol, soft flutter by a "+" symbol and divergence by a "△" symbol.

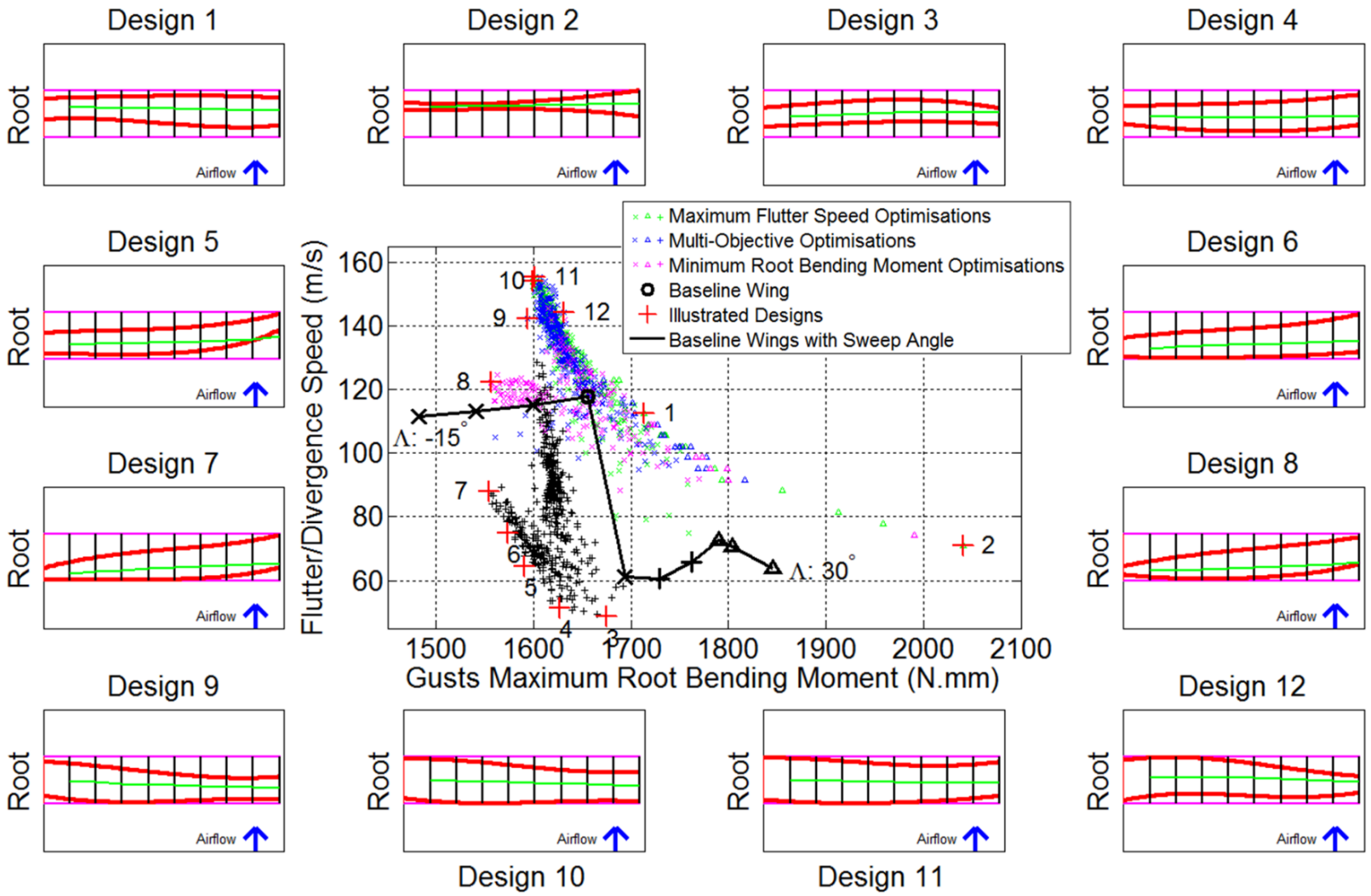

Figure 20. Flutter/Divergence Speed versus Maximum Root Bending Moment during a Worst Case Scenario Gust Event for all Valid Spars Designs with "Free End Points" and Illustration of Spars Designs. The Flutter/Divergence Speed and Root Bending Moment for Wings with Different Sweep Angle (Λ) with a 5° increment are also shown. Hard flutter is identified by a "×" symbol, soft flutter by a "+" symbol and divergence by a "△" symbol.

V. Stringers Planform Geometry

Figure 21 and Figure 24 show the tip displacement versus tip twist for all the valid designs tried under static aerodynamic loading when using the stringers geometry with “fixed end points” and “free end points” respectively. Additionally, the wing structure geometry and flexural axis for different designs are shown including Design 1 to 9 on Figure 21 and Design 1 to 10 on Figure 24 which are designs maximising tip twist for minimum tip displacement. The variation in flexural axis location was increased by 50% to make its variation visible to the reader.

Tip displacement and twist is reduced by at most 0.16% and 2.0% and increased by up to 0.25% and 1.9% with “fixed end points”. Similarly, the tip displacement and twist is reduced by at most 0.14% and 1.8% and increased by up to 0.35% and 2.3% with “free end points” respectively. The variation in tip twist distribution along the span of the wings and the root bending moment are also very small as shown on Figure 23 and Figure 22 for the “fixed end points” results and Figure 26 and Figure 25 for the “free end points” results. At most root bending moment is changed by 0.15% and 0.14% with “fixed end points” and “free end points” respectively.

When considering the static tip load optimisations, for which the data is presented in Appendix I, it was found that varying the stringers geometry has a very small effect on the tip displacement and twist with a maximum variation of up to 0.13% and 0.005° and 0.09% and 0.007° with “fixed end points” and “free end points” respectively.

When considering the maximisation of the natural frequencies for which the data is presented in Appendix I, changing the stringers geometry was found to have once again a very limited effect on the natural frequencies of the wings. At best, changing the stringers geometry can vary the third torsion mode natural frequency by up to 1.2Hz and 1.1Hz. However the effect of the stringers geometry is much smaller on the natural frequency of the lower mode.

Clearly varying the stringers geometry has a very limited effect on the wing tip displacement, twist and root bending moment under aerodynamic loading, tip twist and displacement under a static tip loading and natural frequencies. The improvement in these metrics was considered too weak to justify the computational expense of performing flutter and gusts loads optimisations. Hence these optimisations were not performed.

When considering the geometry of the stringers on Figure 21 and Figure 24 that lead to reduced tip twist and displacement it can be seen that the stringers are curved towards the leading edge of the wing which leads to a reduction in the twisting of the wing under bending load as it places the flexural axis of the wing closer to the load application region (principally around the quarter chord). Hence the stringers geometry mainly acts on the bend-twist coupling of the wing by offsetting the wing stiffness from the load application point similarly to the spars designs found in Section IV.However the stringers geometry has a much smaller effect on the torsional constant of the wing than the one of the spars geometry. Additionally, the stringers are bounded by the spars (i.e. they cannot cross the spars) hence curved stringers have a limited effect as opposed to the curved spars where the spars can reach the edge of the aerodynamic wing. Hence the geometry of the stringers could have an increased effect if their contribution to the wing torsional and bending stiffness was increased (different wing model) or if their design freedom was increased. Similarly the spars planform geometry would have a reduced effect on the wing deformation if their contribution to the torsional and bending stiffness was reduced and/or there design freedom was reduced due to the presence of stringers, extra spars or a need to maintain a certain distance between the spars for fuel volume.

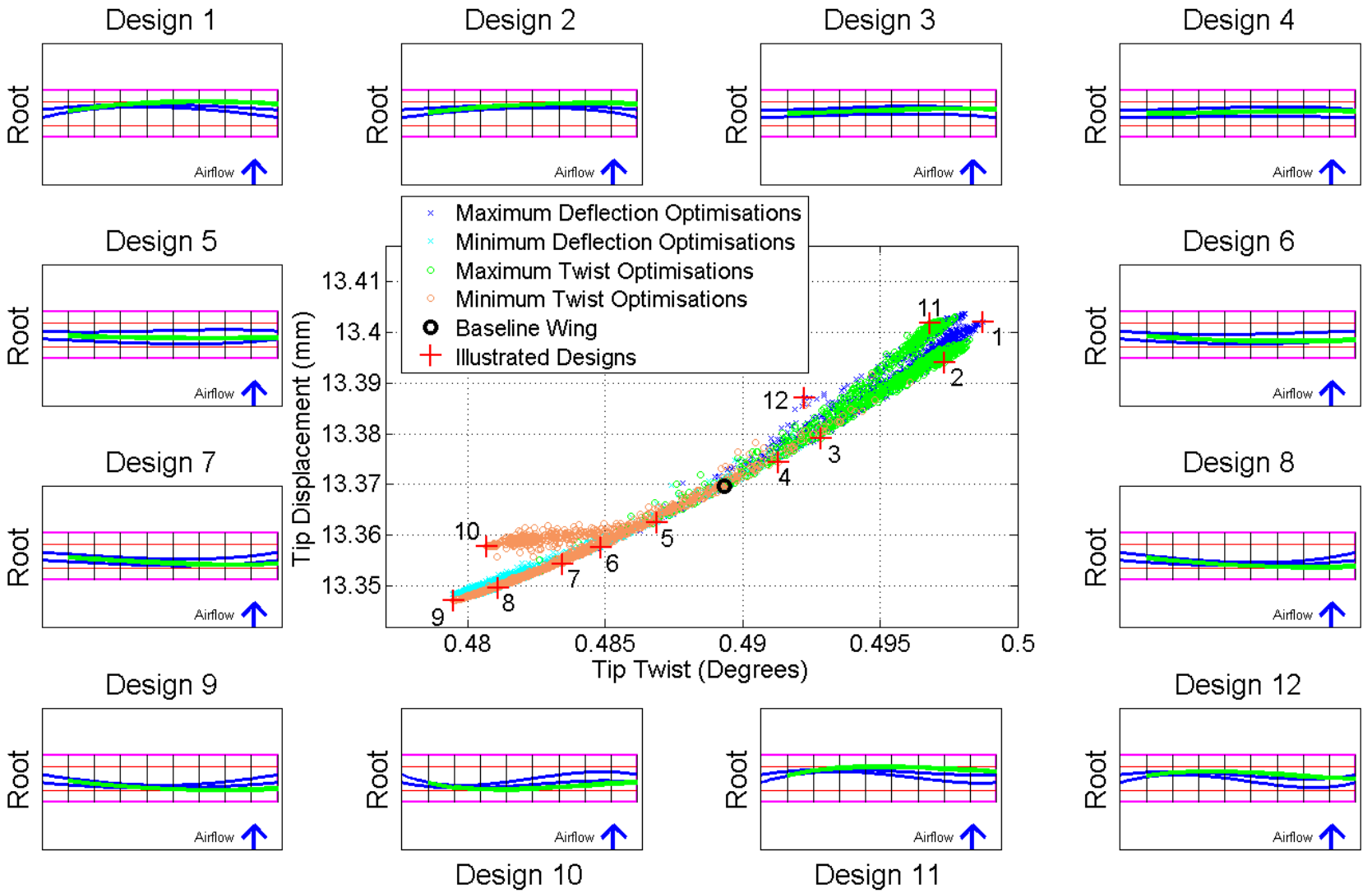

Figure 21. Tip Displacement versus Tip Twist for all Valid Stringers Designs with "Fixed End Points" under Aerodynamic Loading and Illustration of Stringers Designs.

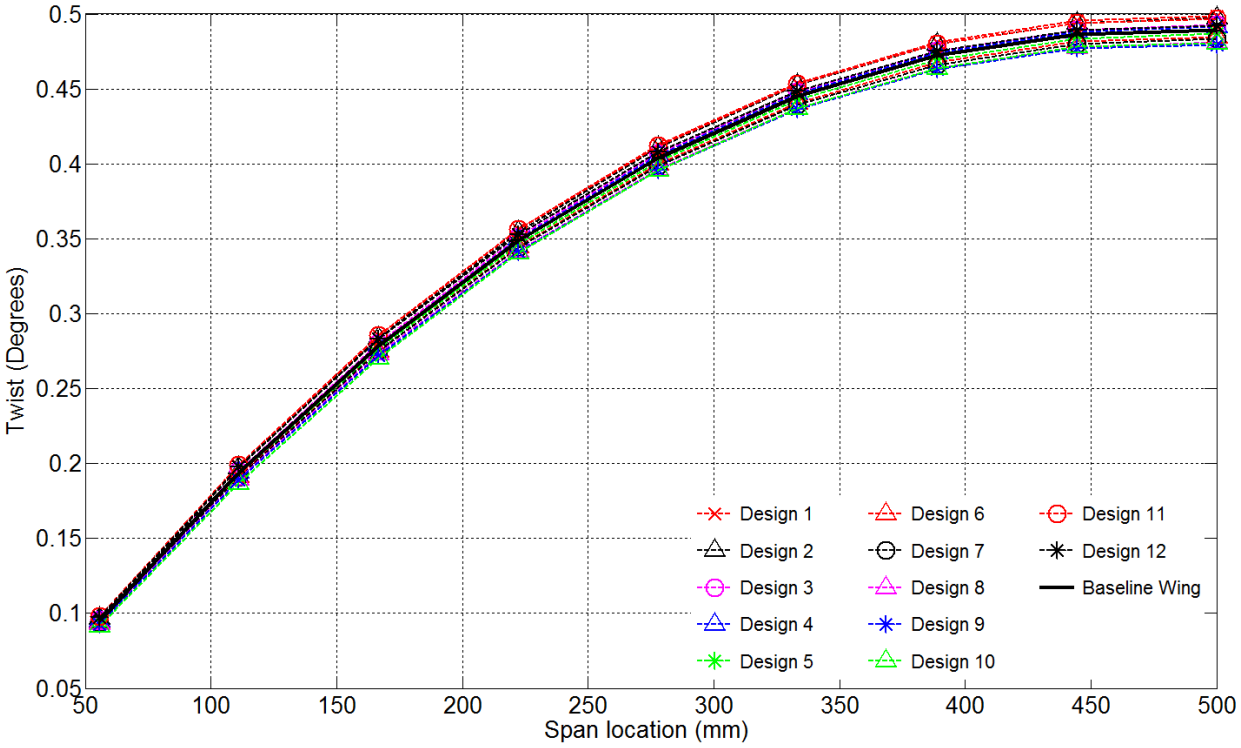

Figure 22. Twist along the Wing Span for the Designs shown on Figure 21.

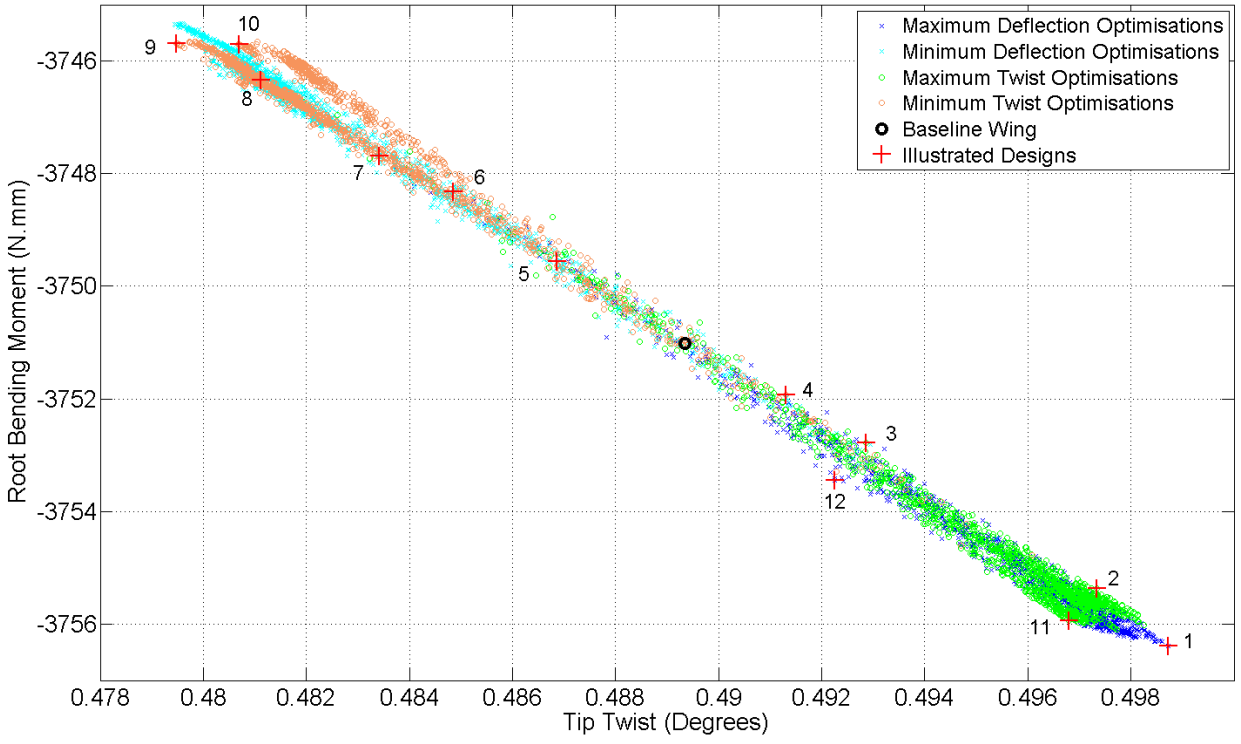

Figure 23. Root Bending Moment versus Tip Twist for all Valid Stringers Designs with "Fixed End Points" under Aerodynamic Loading. The Designs are shown on Figure 21.

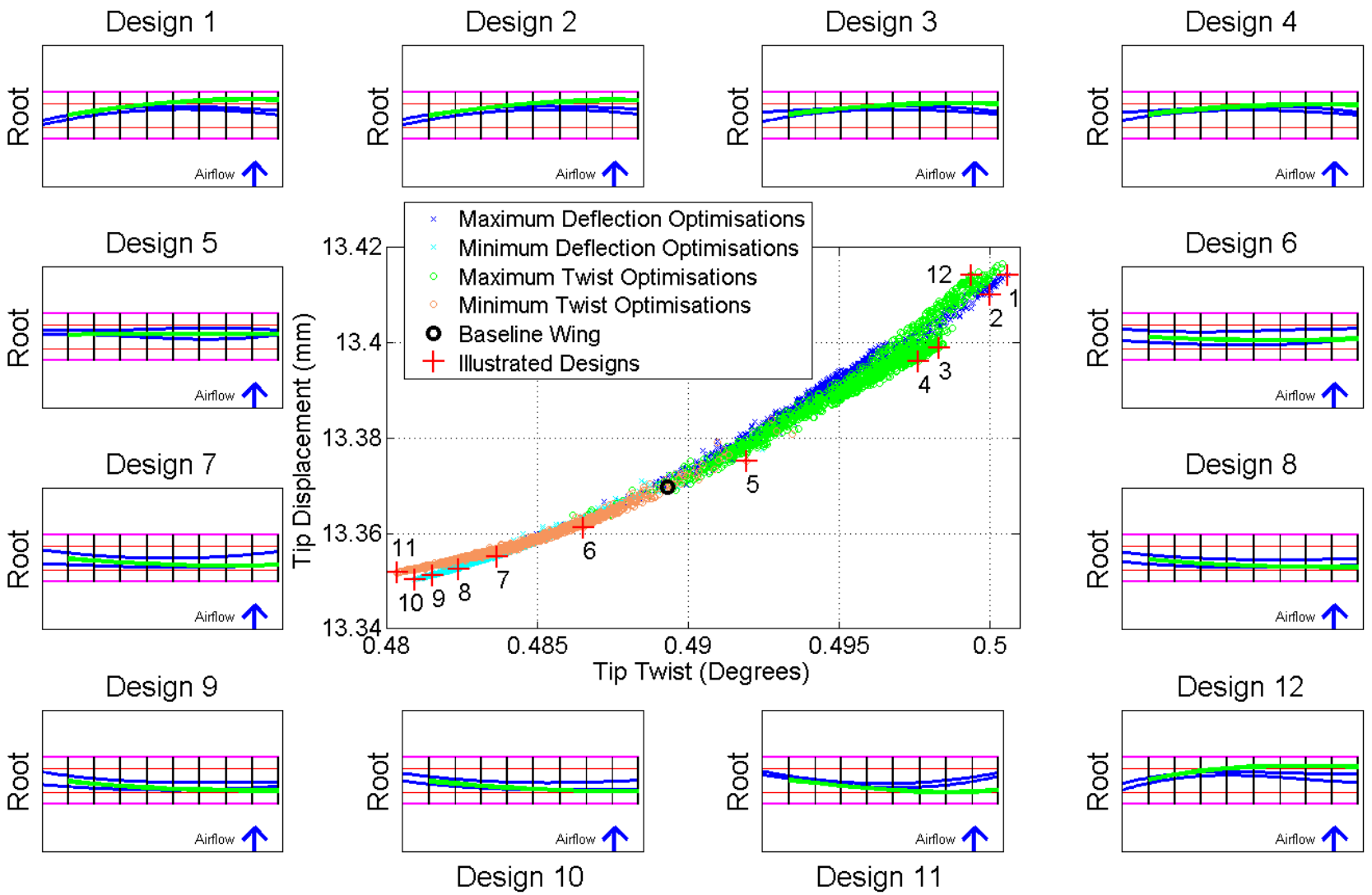

Figure 24. Tip Displacement versus Tip Twist for all Valid Stringers Designs with "Free End Points" under Aerodynamic Loading and Illustration of Stringers Designs.

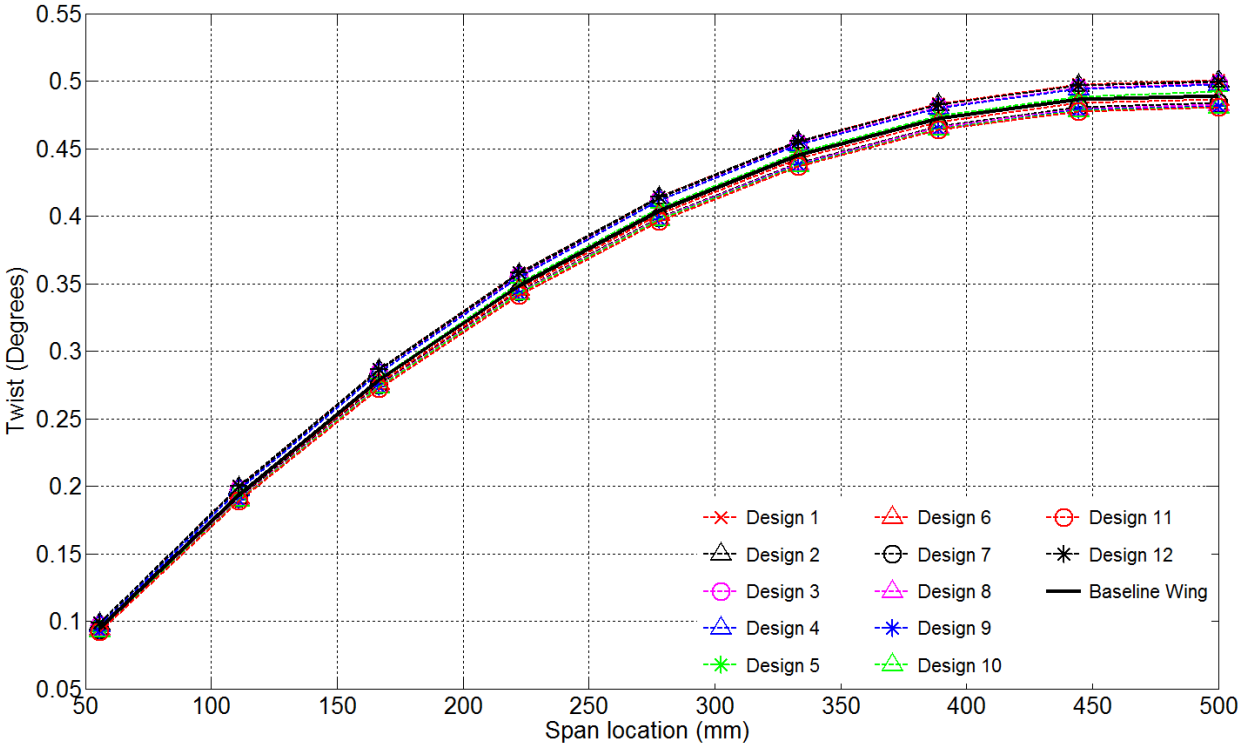

Figure 25. Twist along the Wing Span for the Designs shown on Figure 24.

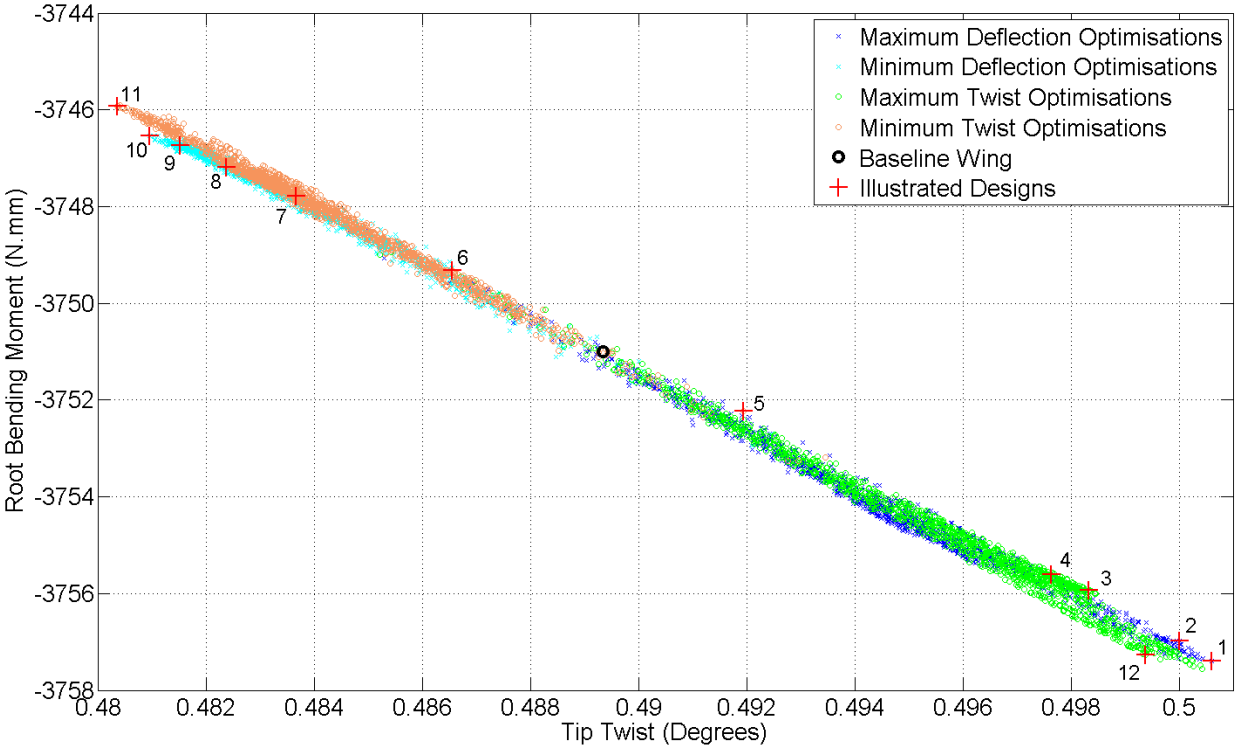

Figure 26. Root Bending Moment versus Tip Twist for all Valid Stringers Designs with "Free End Points" under Aerodynamic Loading. The Designs are shown on Figure 24.

VI. Euler-Bernoulli Beam Model Parameters

A. Euler-Bernoulli Beam Model Parameters Identification

As can be seen in the previous sections the use of the flexural axis to quantify the amount of bend/twist coupling existing in a particular wing concept is complex to implement and also requires a high level of interpretation. In addition changes in the spars planform geometry can lead to not only changes in the bend-twist coupling of the wing but also changes in the wing torsional and bending stiffness. For example, Designs with the lowest root bending moment during the static aeroelastic analysis have spars geometry creating bend-twist coupling and reducing the torsional stiffness however no quantification of each changes has currently been established.

There is a need to use a simpler and more thorough comparison metrics such as the one found in an Euler-Bernoulli beam model, where the bending (w'') and twist (θ') curvature of a uniform beam section is related to the sectional bending moment (M) and torque (T) along the reference axis using

$$\begin{bmatrix} M \\ T \end{bmatrix} = \begin{bmatrix} EI & -K \\ -K & GJ \end{bmatrix} \begin{Bmatrix} w'' \\ \theta' \end{Bmatrix} \tag{10}$$

where EI and GJ are the bending and torsional stiffness parameter and K is the bend/twist coupling parameter. Assuming the y-axis is along the span of the wing, Equation 10 can be rearranged to relate the bending slope (w') and twist (θ) with the first integral of the bending moment and torque using

$$\begin{bmatrix} \int M \\ \int T \end{bmatrix} = \begin{bmatrix} EI & -K \\ -K & GJ \end{bmatrix} \begin{Bmatrix} w' \\ \theta \end{Bmatrix} \tag{11}$$

When dealing with composite materials, K, EI and GJ are a function of the material and cross-section stiffness and can be determined analytically. In the case of geometric bend/twist coupling no such formula exists. Hence to determine the beam properties of a wing with geometric bend/twist coupling 3D FE results under simple load cases can be used to solve a re-arranged form of Equation 11.

For a bending tip load case subject to a tip load P, Equation 11 can be re-arranged as

$$\begin{bmatrix} Py(2\mathrm{L} - \mathrm{y})/2 \\ \int T_B \end{bmatrix} = \begin{bmatrix} EI & -K \\ -K & GJ \end{bmatrix} \begin{Bmatrix} w' \\ \theta \end{Bmatrix} \tag{12}$$

where T_B is the unknown amount of torque created by the off-set of the shear centre due to creation of bend-twist coupling. For a torque T_T load case Equation 11 can be re-arranged as

$$\begin{bmatrix} 0 \\ T_T y \end{bmatrix} = \begin{bmatrix} EI & -K \\ -K & GJ \end{bmatrix} \begin{Bmatrix} w' \\ \theta \end{Bmatrix} \tag{13}$$

Since EI, GJ and K are constant for a given wing section at a given location along the span every load case introduces (at most) one new unknown and two equations hence the number of equations matches the number of unknown with only three load cases: two torque load case and one bending load case.

Assuming that torque value of T_1 and T_2 are used in the first and second load case and a tip load P_3 in the third load case, EI, GJ and K for each section of a design can be found by solving

$$\begin{bmatrix} 0 \\ T_1 y \\ 0 \\ T_2 y \\ P_3 y(2L-y)/2 \\ 0 \end{bmatrix} = \begin{bmatrix} \omega_1' & -\theta_1 & 0 & 0 \\ 0 & -\omega_1' & \theta_1 & 0 \\ \omega_2' & -\theta_2 & 0 & 0 \\ 0 & -\omega_2' & \theta_2 & 0 \\ \omega_3' & -\theta_3 & 0 & 0 \\ 0 & -\omega_3' & \theta_3 & -1 \end{bmatrix} \begin{Bmatrix} EI \\ K \\ GJ \\ \int T_3 \end{Bmatrix} \tag{14}$$

B. Euler-Bernoulli Beam Model Parameters Validation

Using the previous method, *EI*, *GJ* and *K* values at different sections along the wing as shown by Figure 27 for Design 1 of Figure 4. The derived stiffness values are put back into Equation 11 to validate the values obtained. Equation 11 is solved for a bending and a torque load case. The slope and twist for 1D analytical beam and 3D FE are presented in Figure 28 and the maximum difference between the two models is shown on Table 6.

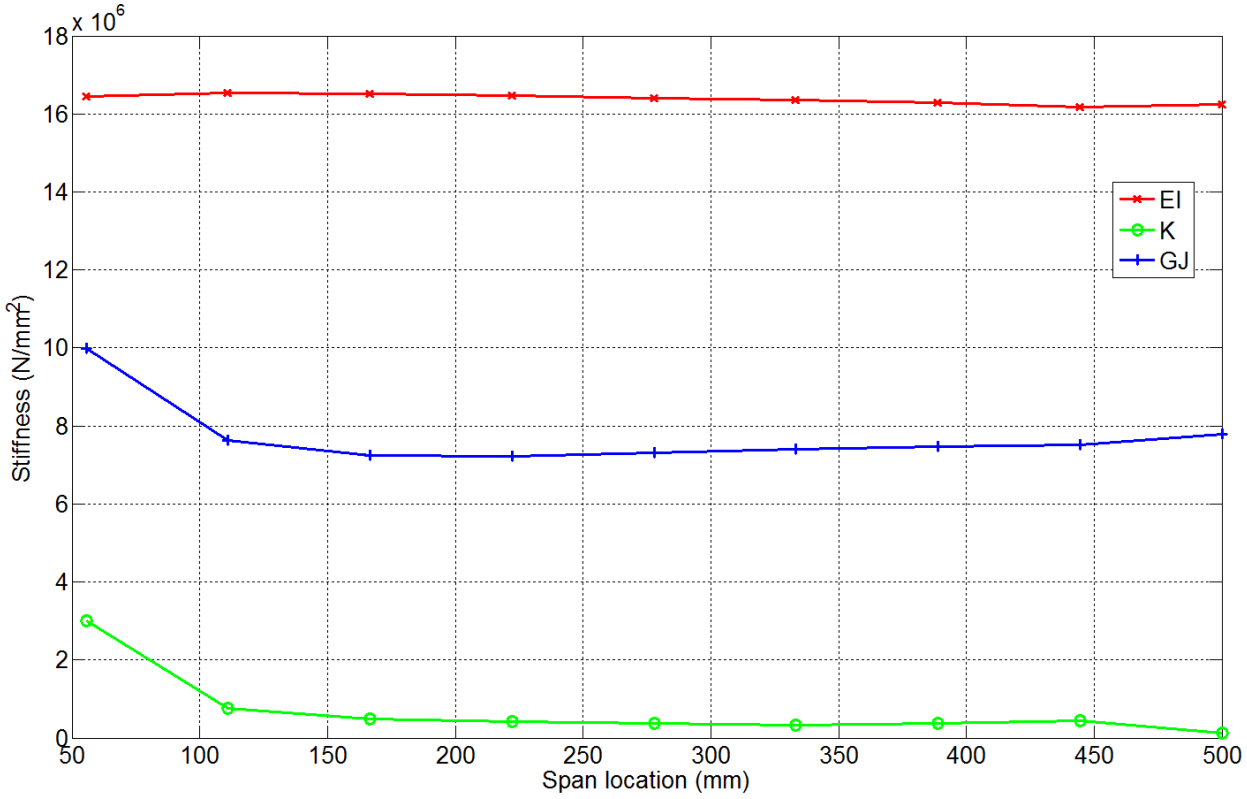

Figure 27. Variation of EI, GJ and K along the Wing Span for Design 1 of Figure 4.

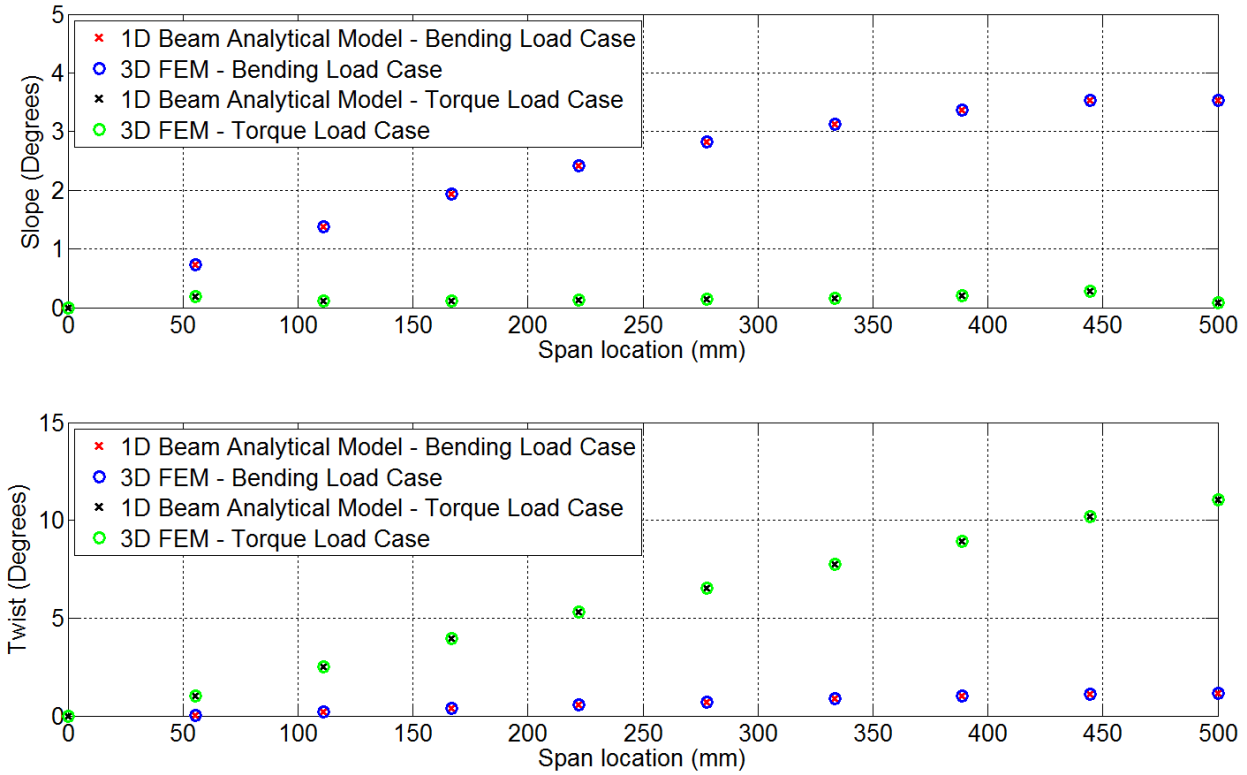

Figure 28. Comparison of the Tip Slope and Twist found by the 1D Analytical Beam and the 3D FE Wing Model for Design 1 of Figure 4.

Table 6. Maximum Percentage Difference in Slope and Twist found by the 1D Analytical Beam and the 3D FE Wing Model for Design 1 of Figure 4.

	Slope	Twist
Maximum Difference - Bending Load Case (%)	0.00	0.00
Maximum Difference - Torque Load Case (%	0.11	0.00

C. Variation of EI, GJ and K with the Spars Planform Geometry

By using the method previously described equivalent Euler-Bernoulli parameters can be identified for the different spars planform geometry found in this paper. The process was carried out for the illustrated designs shown in Section IV with "fixed end points" and "free end points". The same process is also applied to the swept wings previously used to compare the effect of the spars planform geometry to the sweep angle. Figure 29 shows the variation of the equivalent bend-twist coupling parameter for the different designs with respect to the equivalent bending stiffness while Figure 30 shows the variation of the equivalent bend-twist coupling parameter for the different designs with respect to the equivalent torsional stiffness.

Changing the spars planform geometry can lead to large variations in both the torsional stiffness and the bend-twist coupling parameter but only minor variations in the wing bending stiffness. The torsional stiffness of the wing can be increased by up 58.1% and 83.65%, and reduced by up to 42.0% and 58.9% when using "fixed end points" and "free end points", respectively, while the bend-twist coupling parameter can be increased to values similar to one seen on wings swept by around 20°. The bending stiffness is at most changed by -1.9% and -2.0% when using "fixed end points" and "free end points" respectively.

Changing the sweep angle of the wing can reduce the bending and torsional stiffness of the wing by up to 27.9% and 15.0%.

While the sweep angle and the spars planform geometry can have a similar effect on the bend-twist coupling parameter of the wing they have very different effect on the bending and torsional stiffness of the wing. When considering the torsional stiffness it should be noticed that the spars planform geometry offers a much higher control compared to the spar sweep angle both in magnitude and sign. When considering the bending stiffness the spar sweep angle offer higher control than the spars planform geometry in magnitude however this control can only lead to a reduction in the bending stiffness.

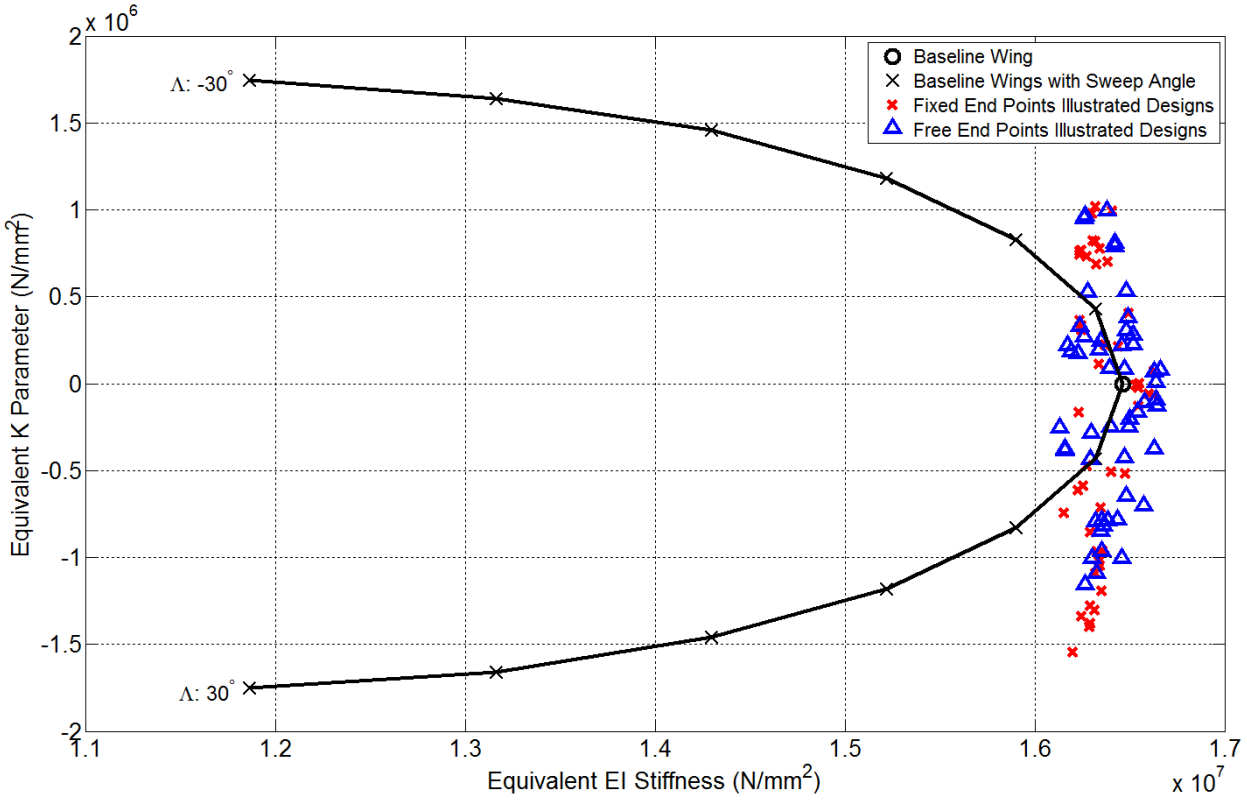

Figure 29. Equivalent Bending Stiffness (EI) and Equivalent Bend-Twist Coupling Parameter (K) for the Illustrated Designs of Section IV and Wings with Different Sweep Angle (Λ) with a 5° increment.

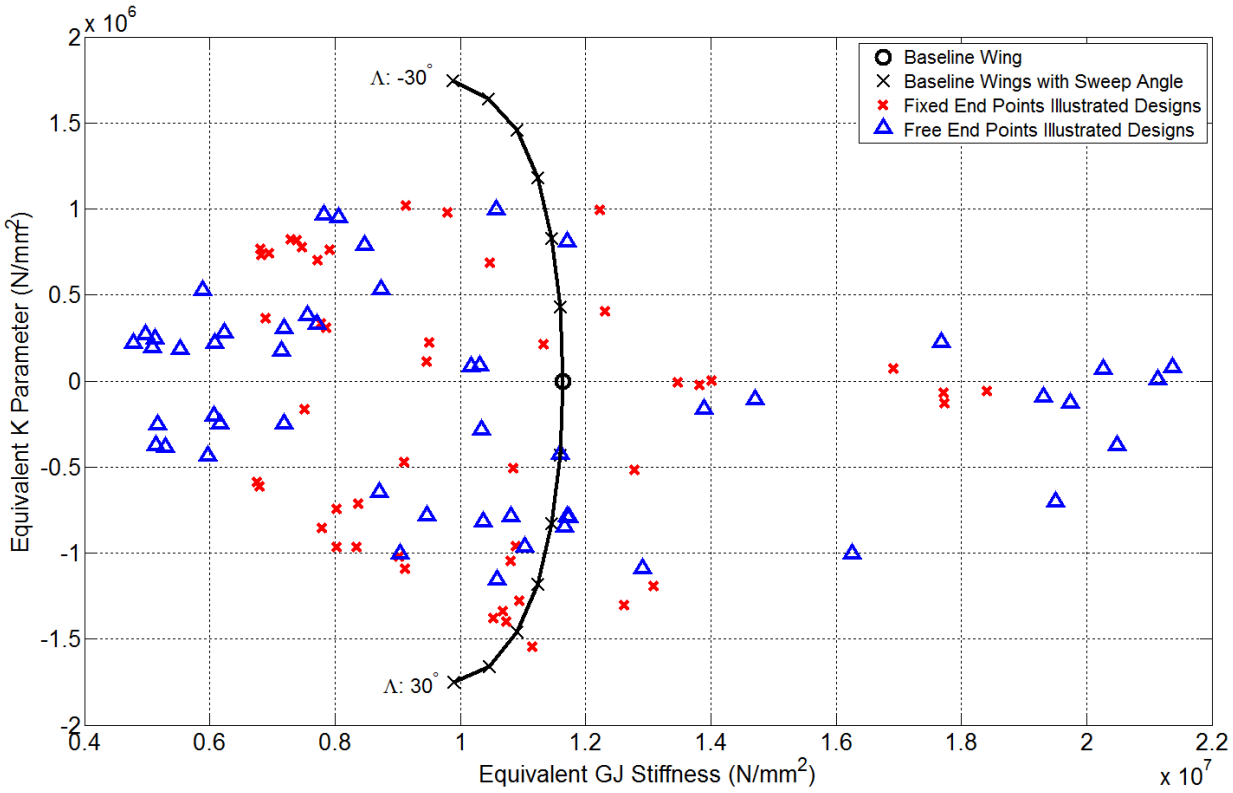

Figure 30. Equivalent Torsional Stiffness (GJ) and Equivalent Bend-Twist Coupling Parameter (K) for the Illustrated Designs of Section IV and Wings with Different Sweep Angle (Λ) with a 5° increment.

VII. Conclusions

In this paper, the effect of changing the spars and stringers planform geometry by modifying their shape and root/tip chord wise location on the wing's static and dynamic aeroelastic behaviour, natural frequencies, flutter/divergence speed and root bending moment during a gust encounter were investigated on an un-tapered un-swept wing model. Overall, the spars planform geometry had a larger effect than the stringers planform geometry at controlling these metrics, e.g. a beneficial variation in instability speed and root bending moment during a gust encounter superior to 25% and 10%.

The control of the spars shape and/or root/tip chord wise location enabled the control of two geometric features of the wing: (1) the overall chord wise location of the spars with respect to the load application point and (2) the minimum chord wise distance separating the leading and trailing edge spar. It was found that only controlling the spars shape achieved the majority of the improvements in the different analysis performed.

Varying the spars planform geometry was found to have a very similar effect to changing the wing sweep angle in the static load cases. When dynamic events are considered a change in the spars shape offers more control on the wing response than a change in wing sweep angle. The capability of the spars planform geometry and the sweep angle to change the wing's deformation was characterised by evaluating the equivalent Euler-Bernoulli beam properties (bending stiffness, torsional stiffness and bend/twist coupling parameter) using a series of prescribed loading cases to the 3D FE models. The values derived highlight the ability of spars shape and root/tip chord wise location to control the wing's bend-twist coupling and torsional stiffness while the spar sweep angle was found to mainly vary the wing's bend-twist coupling and bending stiffness.

Acknowledgments

The author gratefully acknowledges the support of the EPRSC under its ACCIS Doctoral Training Centre grant, EP/G036772/1, the Royal Academy of Engineering and the European Office of Aerospace Research and Development (EOARD). Part of this work was carried out using the computational facilities of the Advanced Computing Research Centre, University of Bristol - http://www.bris.ac.uk/acrc/.

References

1. Airbus. Future Journeys 2013-2032. (2013). Available at: http://www.airbus.com/company/market/forecast/?eID=dam_frontend_push&docID=33752. (Accessed: 8th May 2015)
2. Wright, J. R. & Cooper, J. E. *Introduction to Aircraft Aeroelasticity and Loads*. (Wiley, 2007).
3. Shirk, M. H., Hertz, T. J. & Weisshaar, T. A. Aeroelastic tailoring-theory, practice, and promise. *Journal of Aircraft* **23,** 6–18 (1986).
4. Weisshaar, T. A. Aeroelastic tailoring of forward swept composite wings. *Journal of Aircraft* (1981).
5. Weisshaar, T. A. Aeroelastic tailoring - Creative uses of unusual materials. in *AIAA/ASME/ASCE/AHS 28th Structures, Structural Dynamics and Materials Conference, Monterey, California, April 6-8, 1987* (1987). doi:doi:10.2514/6.1987-976
6. Kim, T. & Hwang, I. H. Optimal design of composite wing subjected to gust loads. *Computers & Structures* **83,** 1546–1554 (2005).
7. Guo, S. Aeroelastic optimization of an aerobatic aircraft wing structure. *Aerospace Science and Technology* **11,** 396–404 (2007).
8. Manan, A., Vio, G. A., Harmin, M. Y. & Cooper, J. E. Optimization of aeroelastic composite structures using evolutionary algorithms. *Engineering Optimization* **42,** 171–184 (2010).
9. Stodieck, O., Cooper, J. E., Weaver, P. M. & Kealy, P. Improved aeroelastic tailoring using tow-steered composites. *Composite Structures* **106,** 703–715 (2013).
10. Maute, K. & Allen, M. Conceptual design of aeroelastic structures by topology optimization. *Structural and Multidisciplinary Optimization* **27,** 27–42 (2004).
11. Stanford, B. K. & Beran, P. Optimal Structural Topology of a Platelike Wing for Subsonic Aeroelastic Stability. *Journal of Aircraft* **48,** 1193–1203 (2011).
12. Stanford, B. K. & Dunning, P. D. Optimal Topology of Aircraft Rib and Spar Structures under Aeroelastic Loads. in *10th AIAA Multidisciplinary Design Optimization Conference, 13-17 January 2014, National Harbor, Maryland, United States of America* 1–23 (2014).
13. James, K. A. & Martins, J. R. R. A. Three-Dimensional Structural Topology Optimization of an Aircraft Wing Using Level Set Methods. in *12th AIAA/ISSMO Multidisciplinary Analysis and Optimization Conference, 10 - 12 September 2008, Victoria, British Columbia Canada* (2008). doi:10.2514/6.2008-6081
14. Brampton, C. J., Kim, H. A. & Cunningham, J. L. Level Set Topology Optimisation of Aircraft Wing Considering Aerostructural Interaction. in *12th AIAA Aviation Technology, Integration, and operations (ATIO) Conference and 14th AIAA/ISSM 17-19 September 2012, Indianapolis, Indiana, United States of America* 1–10 (2012).
15. Dunning, P. D., Brampton, C. J. & Kim, H. A. Multidisciplinary Level Set Topology Optimization of the Internal Structure of an Aircraft Wing. in *10th World Congress on Structural and Multidisciplinary Optimization, Orlando, Florida, United States of America* 1–10 (2013).
16. Dunning, P. D., Stanford, B. K. & Kim, H. A. Aerostructural Level Set Topology Optimization for a Common Research Model Wing. in *10th AIAA Multidisciplinary Design Optimization Conference, 13-17 January 2014, National Harbor, Maryland, USA* 1–21 (2014).
17. Dunning, P. D., Stanford, B. K. & Kim, H. A. Level - Set Topology Optimization with Aeroelastic Constraints. in *56th AIAA/ASMe/ASCE/AHS/SC Structures, Structural Dynamics, and Material Conference, 5 - 9 January 2015, Kissimmee, Florida, USA* 1–19 (2015).
18. James, K. A., Kennedy, G. J. & Martins, J. R. R. A. Concurrent aerostructural topology optimization of a wing box. *Computers and Structures* **134,** 1–17 (2014).
19. Balabanov, V. O. & Haftka, R. T. Topology Optimization of Transport Wing Internal Structure. *Journal of aircraft* **33,** (1996).
20. Kolonay, R. M. & Kobayashi, M. H. Optimization of Aircraft Lifting Surfaces Using a Cellular Division Method. *Journal of Aircraft* **52,** (2015).
21. Sleesongsom, S. & Bureerat, S. New conceptual design of aeroelastic wing structures by multi-objective optimization. *Engineering Optimization* **45,** 107–122 (2013).
22. Vio, G. A., Georgiou, G. & Cooper, J. E. Design of Composite Structures to Improve the Aeroelastic Performance. in *53rd AIAA/ASME/ASCE/AHS/ASC Structures, Structural Dynamics and Materials Conference, 23-26 April 2012, Honolulu, Hawai, United States Of America* 1–13 (2012).
23. Vio, G. A. & Fitzpatrick, I. R. Design of Composite Structures for Improved Aeroelastic Performance. *28th ICAS, 23-28 September 2012, Brisbane, Australia* 1–9 (2012).
24. Locatelli, D., Mulani, S. B. & Kapania, R. K. Supersonic Wing Box Weight Optimization Using Curvilinear Spars and Ribs (SpaRibs). in *51st AIAA/ASME/ASCE/AHS/ASC Structures, Structural Dynamics and Materials Conference, 12-15 April 2010, Orlando, Florida, United States Of America* (2010). doi:10.2514/6.2010-2673
25. Locatelli, D., Mulani, S. B. & Kapania, R. K. Wing-Box Weight Optimization Using Curvilinear Spars and Ribs (SpaRibs). *Journal of Aircraft* **48,** 1671–1684 (2011).
26. Liu, Q., Mulani, S. & Kapania, R. K. Global / Local Multidisciplinary Design Optimization of Subsonic Wing. in *10th AIAA Multidisciplinary Design Optimization Conference, 13-17 January 2014, National Harbor, Maryland, United States of America* 1–17 (2014).
27. Liu, Q., Jrad, M., Mulani, S. B. & Kapania, R. K. Integrated Global Wing and Local Panel Optimization of Aircraft Wing.

in *56th AIAA/ASMe/ASCE/AHS/SC Structures, Structural Dynamics, and Material Conference, 5 - 9 January 2015, Kissimmee, Florida, USA* 1–19 (2015).

28. Jutte, C. V., Stanford, B. K., Wieseman, C. D. & Moore, J. B. Aeroelastic Tailoring of the NASA Common Research Model via Novel Material and Structural Configurations. in *55th AIAA/ASMe/ASCE/AHS/SC Structures, Structural Dynamics, and Material Conference, 13 - 17 January 2014, National Harbor, Maryland, USA* 1–20 (2014).
29. Francois, G. & Cooper, J. E. Novel Structural Wing Designs for Forward Swept Wings. in *2014 Royal Aeronautical Society Biennial Applied Aerodynamics Research Conference, 22-24 July 2014, Bristol ,UK* 1–16 (2014).
30. Francois, G., Cooper, J. E. & Weaver, P. M. Aeroelastic Tailoring of Composite Wings using Internal Structural Members Shape and Stacking Sequence. in *4th Aircraft Structural Design Conference, 7-9 October 2014, Belfast, United Kingdom* (2014).
31. Francois, G., Cooper, J. E. & Weaver, P. M. Impact of the Wing Sweep Angle and Rib Orientation on Wing Structural Response for Un-Tapered Wings. in *57th AIAA/ASMe/ASCE/AHS/SC Structures, Structural Dynamics, and Material Conference, 4 - 8 January 2016, San Diego, California, USA* (2016). doi:10.2514/6.2016-0472
32. Francois, G., Cooper, J. E. & Weaver, P. M. Aeroelastic Tailoring using Rib / Spar Orientations : Experimental Investigation. in *56th AIAA/ASMe/ASCE/AHS/SC Structures, Structural Dynamics, and Material Conference, 5 - 9 January 2015, Kissimmee, Florida, USA* 1–22 (2015).
33. Francois, G., Cooper, J. E. & Weaver, P. M. Aeroelastic tailoring using crenellated skins – modelling and experiment. *Advances in Aircraft and Spacecraft Science* **4,** (2017).
34. Tatham, R. Shear Centre, Flexural Centre and Flexural Axis: An Attempt to Clear up Current Confusion and Provide Definitions Differentiating Between the Three Terms. *Aircraft Engineering and Aerospace Technology* **23,** 209–210 (1951).
35. Stodieck, O., Cooper, J. E. & Weaver, P. M. On the Interpretation of Bending-Torsion Coupling for Swept, Non-Homogenous Wings. in *56th AIAA/ASMe/ASCE/AHS/SC Structures, Structural Dynamics, and Material Conference, 5 - 9 January 2015, Kissimmee, Florida, USA* 1–28 (2015).
36. Samareh, J. A. A survey of shape parameterization techniques. in *CEAS/AIAA/ICASE/NASA Langley International Forum on Aeroleasticity and Structural Dynamics, 22 - 25 June 1999, Williamsburg, Virginia, United States of America* 333–343 (1999).
37. Kennedy, J. & Eberhart, R. Particle swarm optimization. in *IEEE International Conference on Neural Networks, Perth, WA* **4,** 1942–1948 (Ieee, 1995).
38. Parsopoulos, K. E. & Vrahatis, M. N. Particle swarm optimization method for constrained optimization problems. in *In Proceedings of the Euro-International Symposium on Computational Intelligence 2002* (2002).
39. Mazhoud, I., Hadj-Hamou, K., Bigeon, J. & Joyeux, P. Particle swarm optimization for solving engineering problems: A new constraint-handling mechanism. *Engineering Applications of Artificial Intelligence* **26,** 1263–1273 (2013).
40. Rodden, W. P. & Johnson, E. H. *MSC/NASTRAN Aeroelastic Analysis User's Guide v68*. (The MacNeal-Schwendler Corporation, 1994).
41. Johnson, E. H. MSC Developments in Aeroelasticity. in *1997 MSC Aerospace Users' Conference* 1–9 (1997).
42. Khodaparast, H. H. *et al.* Rapid Prediction of Worst Case Gust Loads. in *52nd AIAA/ASME/ASCE/AHS/ASC Structures, Structural Dynamics and Materials Conference, 4-7 April 2011, Denver, Colorado, United States Of America* 1–22 (2011). doi:10.2514/6.2011-2040

Appendix I

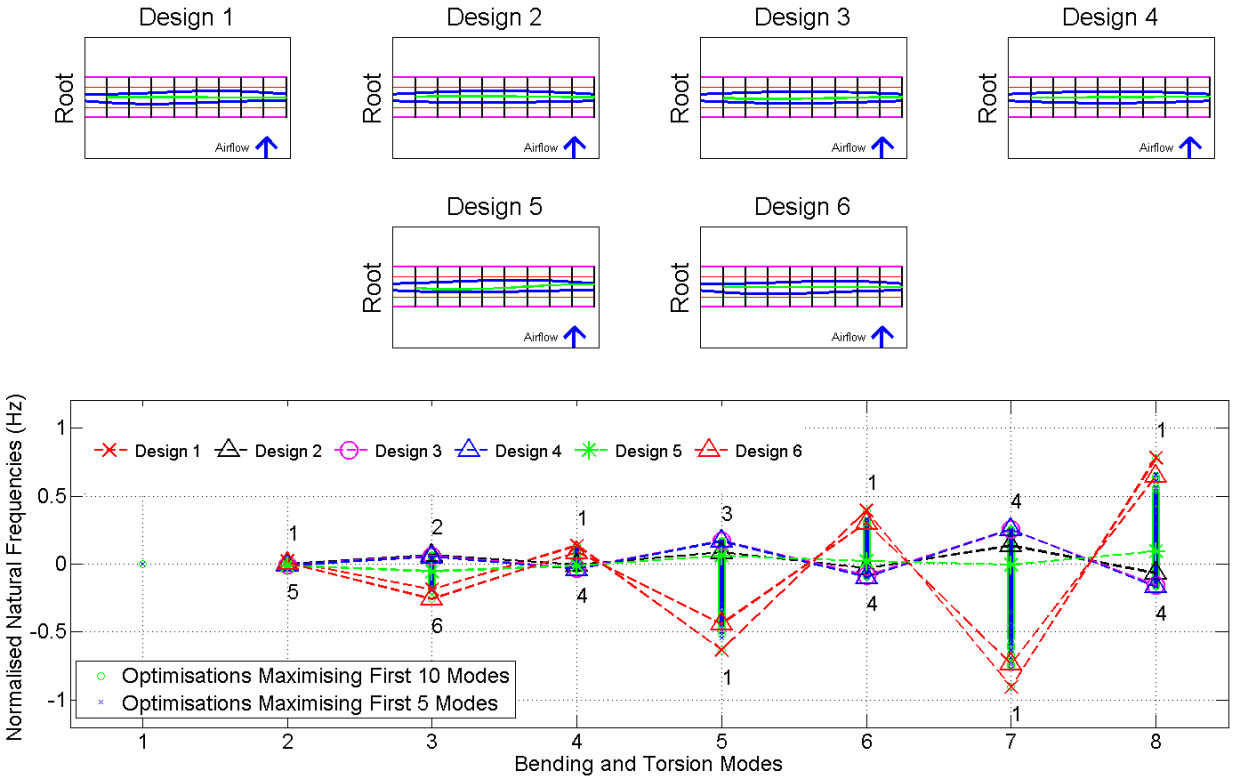

Figure A. Normalised Natural Frequencies of the First Eight Modes of each Valid Stringers Designs with "Fixed End Point" and Stringers designs Maximising Variation with the Baseline Values for each Mode.

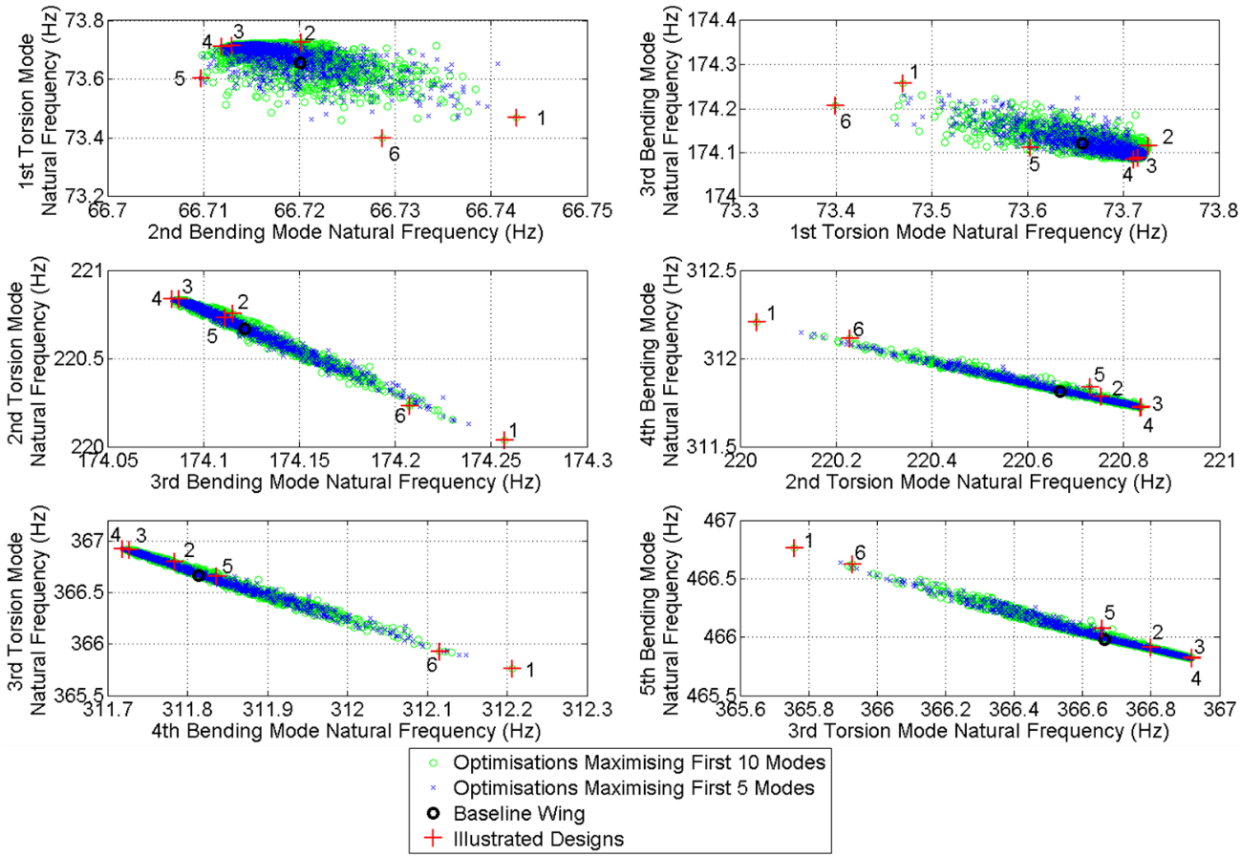

Figure B. Natural Frequencies Variation for Mode 2 to 8 of each Valid Stringers Designs tried with "Fixed End Points". The Numbers Refer to the Designs shown in Figure A.

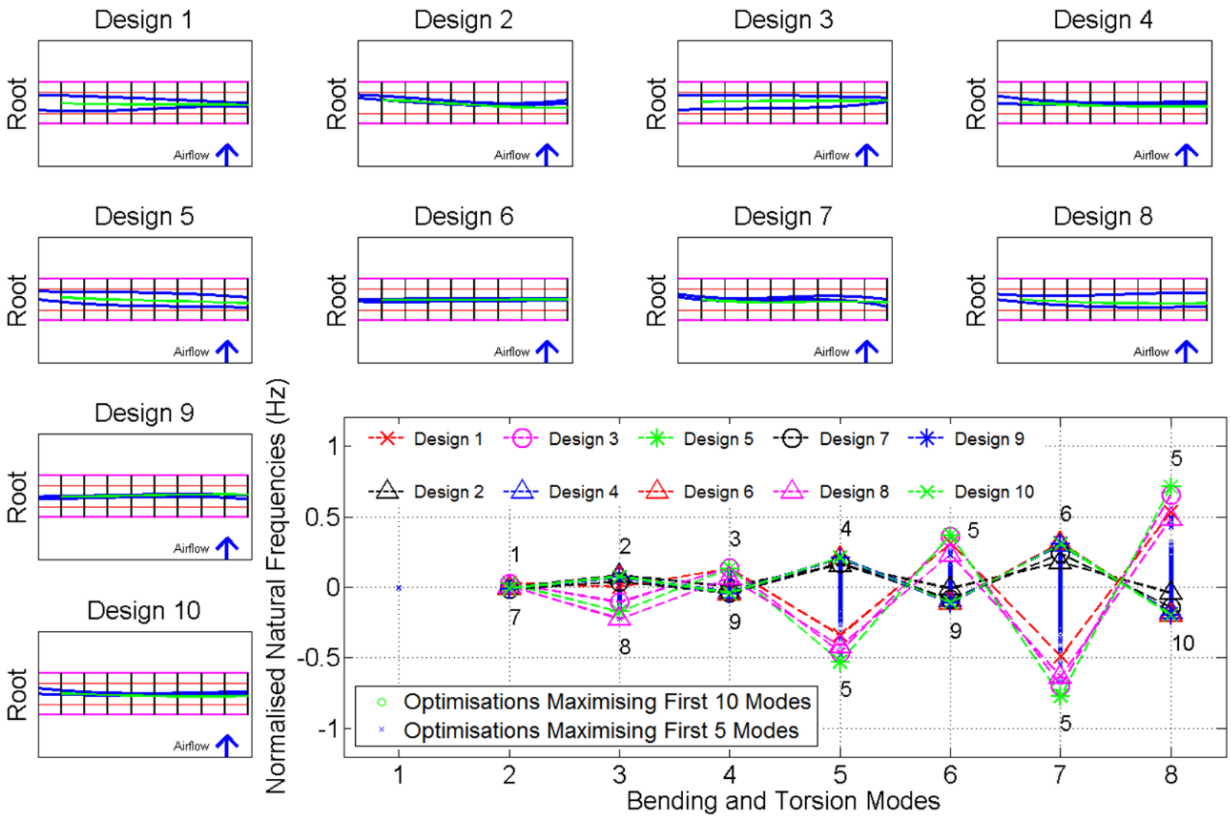

Figure C. Normalised Natural Frequencies of the First Eight Modes of each Valid Stringers Designs with "Free End Point" and Stringers designs Maximising Variation with the Baseline Values for each Mode.

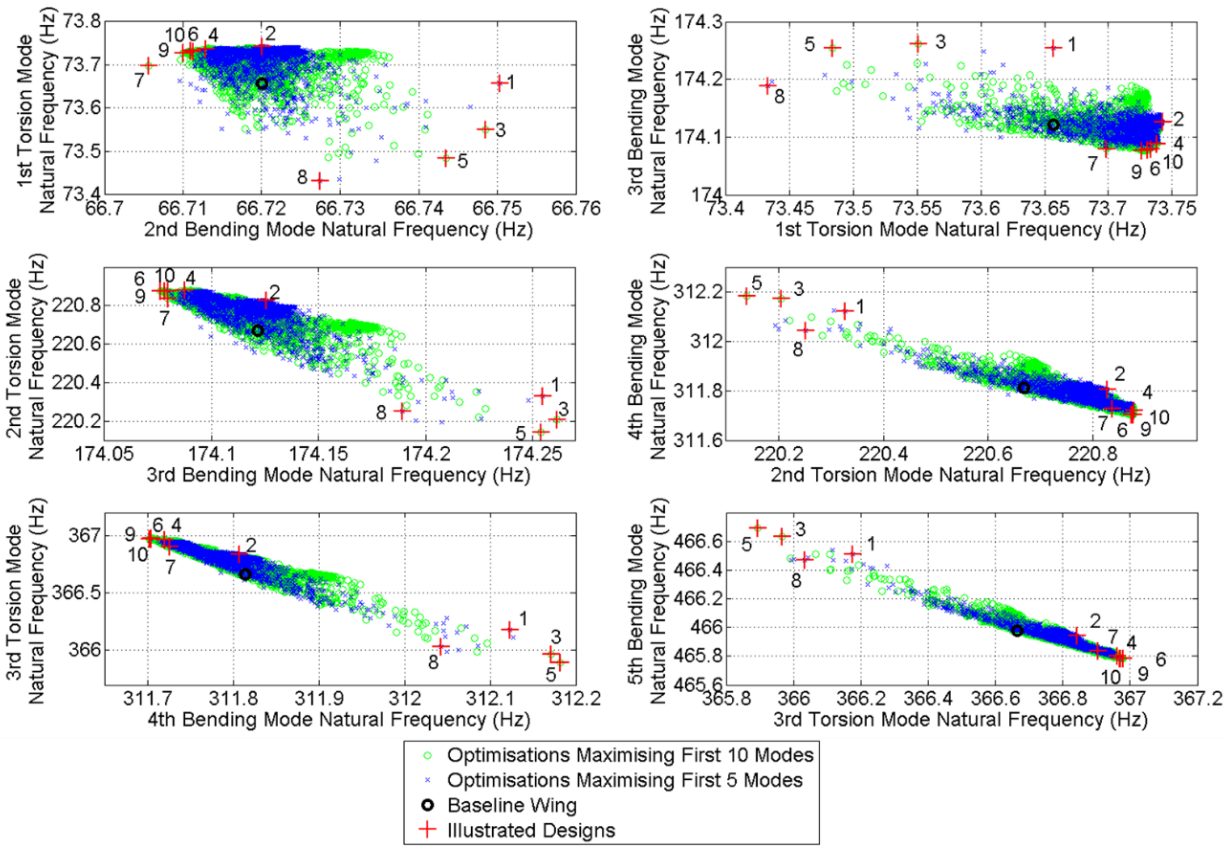

Figure D. Natural Frequencies Variation for Mode 2 to 8 of each Valid Stringers Designs with "Fixed End Points". The Numbers Refer to the Designs shown in Figure C.

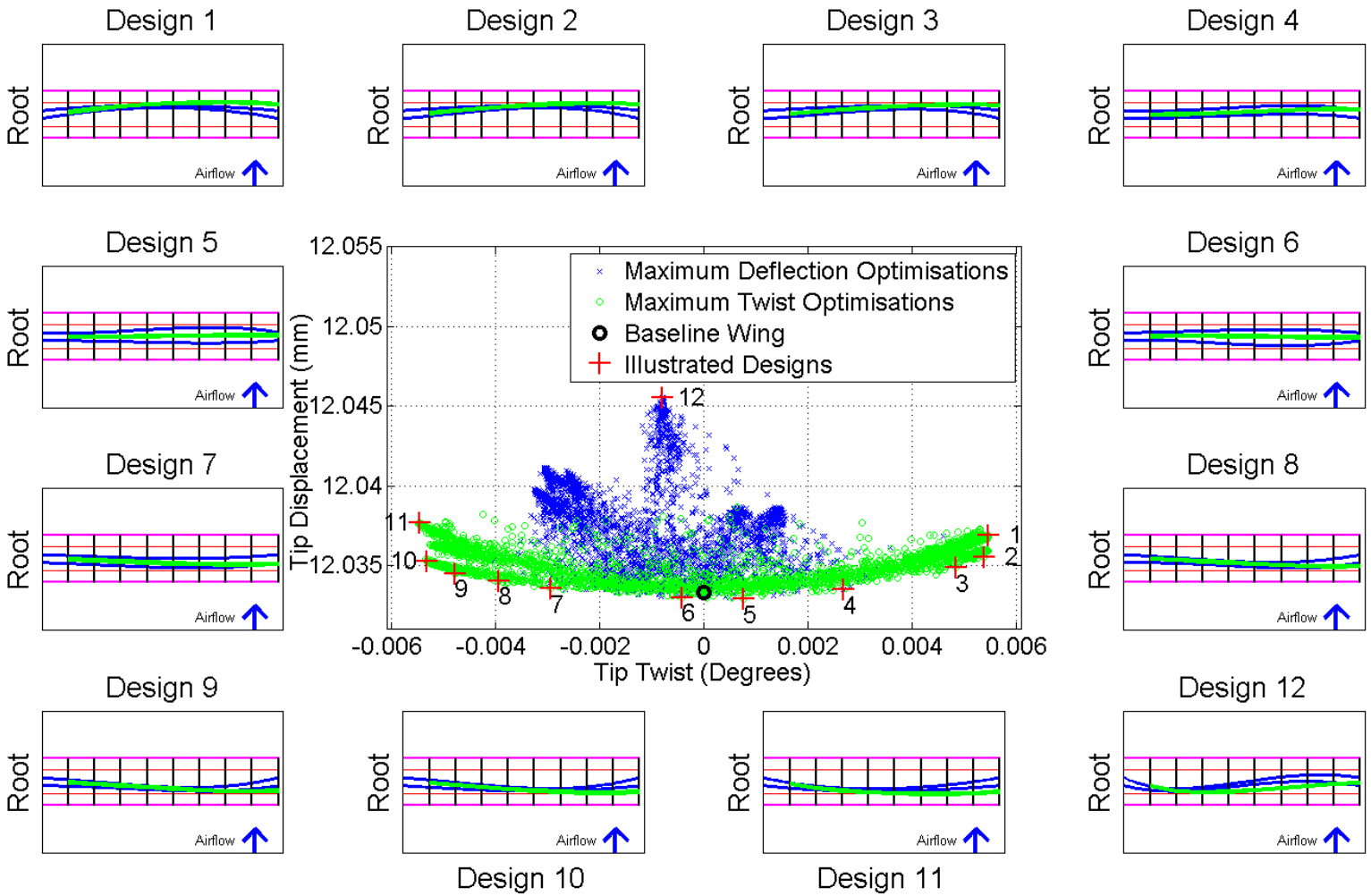

Figure E. Tip Displacement versus Tip Twist for all Valid Stringers Designs with "Fixed End Points" under a Tip Load and Illustration of Stringers Designs. The Flexural Axis Variation is increased by 50%.

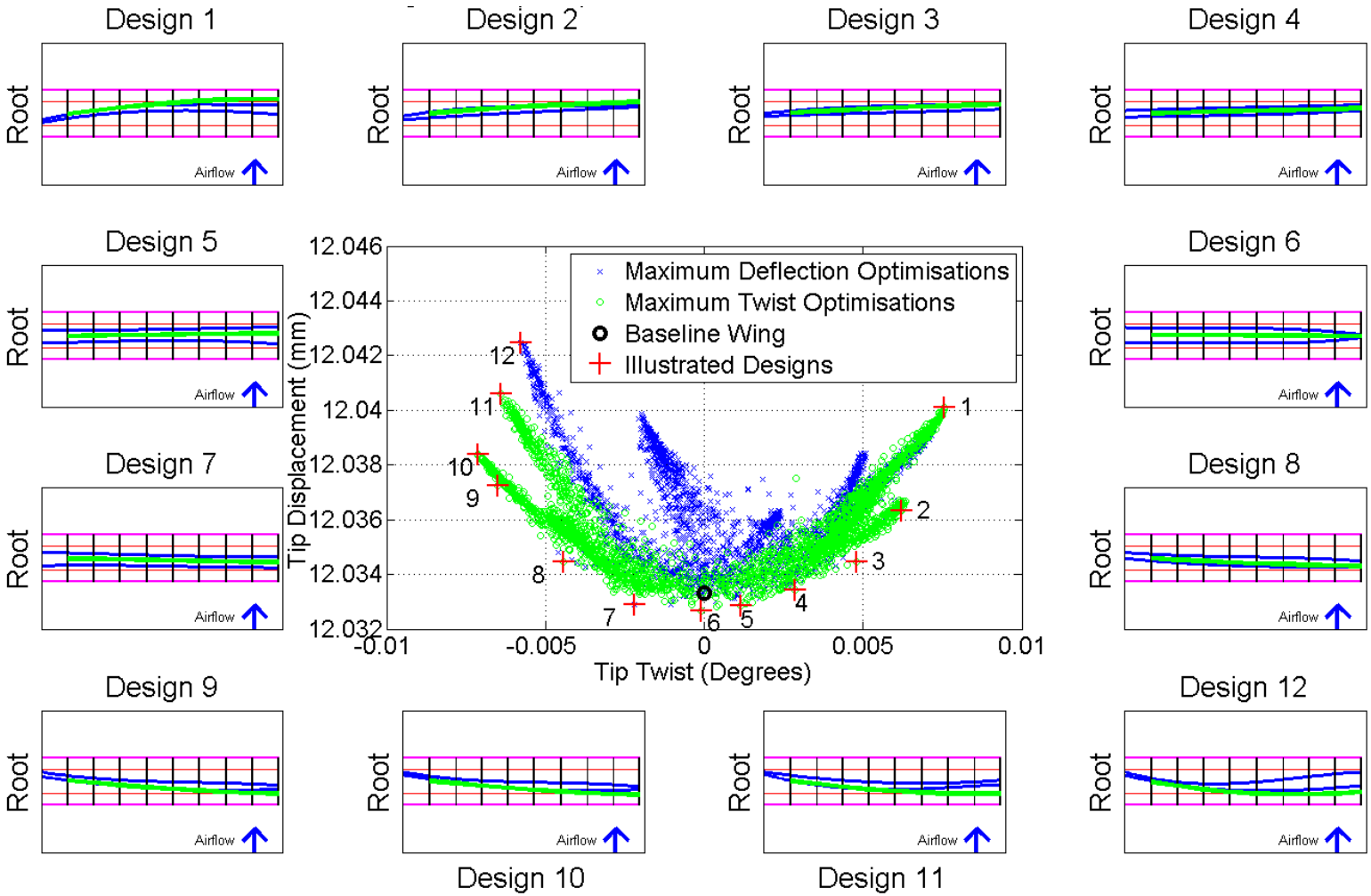

Figure F. Tip Displacement versus Tip Twist for all Valid Stringers Designs with "Free End Points" under a Tip Load and Illustration of Stringers Designs. The Flexural Axis Variation is increased by 50%.